



ANALYSIS OF PHOTONIC SWITCHING BASED ON Si/GST TECHNOLOGY

Author: Alejandro Santomé Valverde

Supervisor: Pablo Sanchis Kilders

Co-supervisor: Jorge Parra Gómez

Starting date: 08/02/21

Workplace: Nanophotonics Technology Center (NTC) of Valencia

Master's Thesis presented at Escuela Técnica Superior de Ingeniería de Telecomunicación (ETSIT) of Universitat Politècnica de València, to obtain the title "Máster Universitario en Tecnologías, Sistemas y Redes de Comunicaciones".

Course 2020-21

Valencia, 3 July 2021



Objectives — The main objective of this Master's Thesis is to analyse, through both simulations and experiments, hybrid Si/GST waveguides featuring high-performance for optical switching with a non-volatile response.

Methodology — First, the optical performance of the hybrid waveguide and ring resonators with the optimal thickness of the GST layer are analysed by means of simulations for the GST in the amorphous and crystalline states. All calculations are obtained and optimized for the transverse electric (TE) and transverse magnetic (TM) polarization at 1550 nm. Based on such results, a sample with waveguides and ring resonators is fabricated. The optical losses of such structures are measured at telecom wavelengths to determine the change on both phase and absorption when the GST is in each state. Crystallization is achieved by rapid thermal annealing at 250 °C in N₂ for 10 min. Finally, all-optical and non-volatile switching is demonstrated in both waveguides and rings by using nanosecond optical pulses.

Theoretical developments — The optical modes and associated effective refractive index values are calculated by using a finite element method (FEM) mode solver. The optimal lengths of the GST patches used in straight waveguides and ring resonators are obtained. The optical response of a ring resonator is investigated in terms of the coupling coefficient and extinction ratio to achieve a measurable phase shift in the amorphous and crystalline state.

Prototype design and laboratory work — A sample with hybrid Si/GST waveguides and ring resonators was fabricated. The optical response of the structures was measured with the GST in the amorphous and crystalline state. A setup for on-chip all-optical switching at telecom wavelengths is mounted. All-optical switching is carried out. Optical inspection of the hybrid waveguides during the characterisation process is done by means of an optical microscope.

Results — Experimental characterisation shows good agreement with simulation values. Both large extinction ratios and phase shifts of around 5 dB/μm and $\pi/2$ rad/μm, respectively, have been measured. All-optical switching has been achieved for the amorphization and crystallization process with switching energies as low as sub-nanojoules. A non-volatile response has been demonstrated showing the possibility of achieving intermediate losses by changing gradually the GST layer.



Future working lines — To characterize the all-optical switching in the time domain. Optimize the shape of the optical pulses for crystallization. Investigate the performance of Si/GST waveguides covered with a SiO₂ cladding.

Publications — The main results of this work were presented as ePoster in the Spintronics, Photonics, Phononics or Magneto-Optics Online International Conference (SPPM 2021) celebrated on June 10.

A. Santomé, H. Urgelles-Pérez, J. Parra, and P. Sanchis, “High-performance optical switches based on GST/Si waveguides,” in 1st Spintronics, Photonics, Phononics or Magneto-Optics Online International Conference (SPPM 2021), Online, 2021, pp. 35-35.

Abstract — The integration of the GST (germanium-antimony-tellurium or GeSbTe) material into silicon structures enables non-volatile switching between two states upon application of an optical excitation. This switching originates from the transition of the GST material between an amorphous and crystalline state which allows varying the absorption and phase of the optical signal propagating through hybrid Si/GST guides. The aim of this master's thesis is to experimentally demonstrate and analyse the photonic switching performance achievable by guided structures based on the combination of silicon and GST. To this end, silicon waveguides and ring resonators with GST are fabricated and characterized. Our results show high performance in ultra-compact footprints. Both large extinction ratios and phase shifts of around 5 dB/ μm and $\pi/2$ rad/ μm , respectively, have been measured. On the other hand, on-chip all-optical switching is achieved by using nanosecond optical pulses and switching energies as low as sub-nanojoules. Our devices may find applications in a wide range of fields, such as optical memories, ultra-low power switching or neuromorphic computing.

Author: Alejandro Santomé Valverde, email: alsanva3@teleco.upv.es

Supervisor: Pablo Sanchis Kilders, email: pabsanki@ntc.upv.es

Co-supervisor: Jorge Parra Gómez, email: jorpargo@ntc.upv.es

Delivery date: 03/07/21



TABLE OF CONTENTS

I. Introduction and review of the state of the art	5
I.1 Importance and current status of silicon-based integrated photonics - applications	5
I.1.1 Introduction to silicon photonics	5
I.2 Introduction to GST and its properties	7
I.2.1 Phase Change Materials	7
I.2.2 GST	7
I.3 Review of the state of the art of devices based on Si/GST technology. Functionalities and possible applications.....	7
II. Objectives and methodology	10
II.1 Objectives.....	10
II.2 Methodology	10
III. Design of Si/GST hybrid waveguides and switching techniques	11
III.1 Design of Si/GST hybrid waveguides	11
III.2 Design and simulation of validation photonic structures	14
III.2.1 Structures to determine the propagation losses: straight hybrid waveguides	14
III.2.2 Structures to analyse the phase shift variation: optical ring resonators.....	14
III.3 Review of switching techniques.....	18
III.3.1 Electrical switching	18
III.3.2 All-optical switching	18
III.3.3 Comparison between optical and electrical switching	20
IV. Experimental results	21
IV.1 Design of GDS and description of fabrication process	21
IV.1.1 Design of GDS	21
IV.1.2 Fabrication process.....	22
IV.1.3 Images of the fabricated sample and fabrication discrepancies	23
IV.2 Definition of characterisation process.....	24
IV.2.1 Characterisation of the sample: propagation losses and phase shift variation	24
IV.2.2 Setup for all-optical switching	25
IV.3 Characterisation of absorption switching	26
IV.3.1 Images of the waveguides for propagation loss characterisation	26
IV.3.2 Comparison of absorption between amorphous and crystalline	26
IV.3.3 All-optical switching	29
IV.4 Characterisation of phase switching.....	31



IV.4.1	Images of ring resonators for phase shift characterisation	31
IV.4.2	Analysis of phase shift variation between amorphous and crystalline	32
IV.4.3	All-optical switching	35
V.	Conclusions and future work	36
V.1	Conclusions	36
V.2	Future work	36
	References.....	37
	Appendix I. Poster for SPPM2021 international online conference	39

I. Introduction and review of the state of the art

The term photonics defines the physical science and application of light (photon) generation, detection, and manipulation through emission, transmission, modulation, signal processing, switching, amplification, and sensing. Photonics became popular when optical telecommunication systems appeared, where the signals are guided over optical transmission lines instead of copper wire pairs and coaxial cables. This was possible due to the invention of first practical semiconductor light emitters, in the early 1960s, and optical fibres, developed in the 1970s. Therefore, tasks that were previously carried out by electronics are now implemented in photonic systems.

Photonics technology includes light sources (lasers and LEDs), waveguides and some other optoelectronic devices that are in charge to encode digital information onto optical signals and convert optical signal to electrical ones. The components mentioned before are typically discrete. However, in several applications it is necessary for components to be directly coupled to each other. For this reason, integrated photonics emerged as a branch of photonics in which waveguides and other devices are fabricated as an integrated structure on a common planar substrate [1].

Analogous to the way electronics has miniaturised components, integrated photonics is pursuing the same goal. This is possible due to the wavelength of the light, which combined with the utilization of high-index materials permits ultra-compact micron-size photonic devices. The frequency of light is significantly higher than the values used in radiofrequency. Therefore, the bandwidth is larger, which increases the bit rate [2].

Integrated photonics have advanced slower than integrated electronics in terms of integration density. Considering the number of devices in an integrated photonics chip, they are of the order of hundreds or thousands. On the other hand, an electronic integrated circuit can contain around a billion transistors [3]. In order to increase the number of devices in a photonic integrated circuit (PIC), researchers have focused on the different properties of the materials used to fabricate these chips. Considering the importance of the refractive index, there is a class of materials with interesting properties that will be analysed in this work, the phase change materials.

I.1 Importance and current status of silicon-based integrated photonics - applications

I.1.1 *Introduction to silicon photonics*

Silicon-based devices are interesting for a combination of technological and cost reasons. In terms of cost, silicon and Silicon-on-Insulator (SOI) wafers are much cheaper than devices made with combinations of III-V materials, such as lithium niobate (LiNbO_3), gallium arsenide (GaAs) or indium phosphide (InP) [4]. Depending on the application, each material will suit better. For example, GaAs or InP are mainly used for lasers and photodetectors, whereas LiNbO_3 is used for modulators. The problem is that these materials are not easy to integrate all together in the same PIC. Thus, a low-cost material where components are easy to integrate is required.

Silicon photonics (SiPh) is a promising platform in order to overcome the issue mentioned before because of its advantages over other substrates. One important characteristic is the high index contrast between Si and SiO_2 (silica), enabling the miniaturization of devices. Moreover, the generation of this kind of structure is cheap and it has been widely used in the micro-electronic field. Although, the most interesting property is the compatibility with CMOS technology. This fact enables the fabrication of both electronic and photonic devices in the same chip, reaching submicron dimensions and bending radius in the order of micrometres.

The first product using silicon photonics was released in 1998 by the UK-based optical manufacturer Bookham Technology Ltd [5] and, from that moment, optical communications have been the main application for silicon photonics. Nevertheless, before unveiling their first product,

they were researching for almost 10 years on the possibility of using SOI wafers. SOI provided a planar thin-film structure that can guide the light in the top silicon layer. However, they found an issue which was that the layer must not be thicker than approximately 200 nm in order to avoid multimodal behaviour. For this reason, they had to research on this field to fulfil the requirements they had stipulated for the guiding structure: single mode, polarization independent and producible using conventional processes. As an example of the mentioned research, a passive optical network transceiver designed by Bookham in 1993 is shown in Fig. 1.

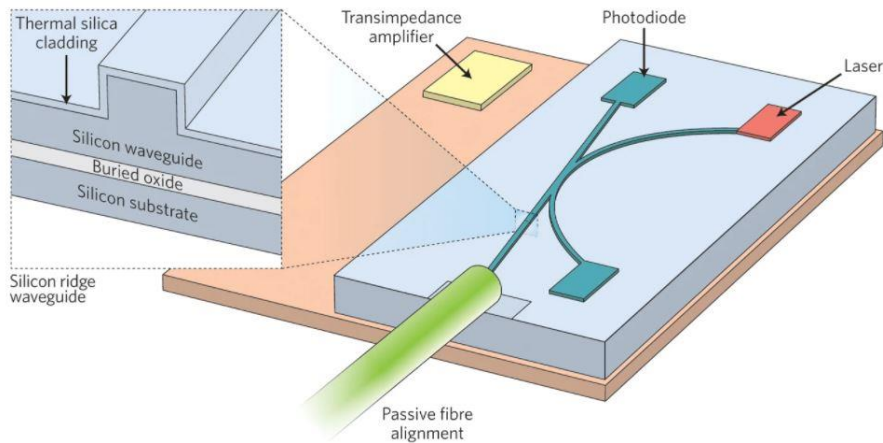


Fig. 1. PON transceiver made by Bookham in 1993 [5].

The growth of interest in silicon photonics technology was accentuated by the inclusion of Cisco and Intel in the market. However, another company called Kotura Inc. converted itself in the leading commercial silicon photonic company in terms of revenue, shipped channels and gross margins [5]. They considered that with internet traffic set to grow significantly for the foreseeable future, silicon photonics combined with optical fibre communication would be the solution for data centers in order to face the escalating of power consumption, latency, operation costs or wiring density. Years before, their considerations were proven to be correct.

Despite the large number of advantages, silicon has well-known shortcomings in terms of light generation [6] at any band and light detection in the telecommunication band. It also has problems with non-linearities. One of them is that silicon lacks second-order optical nonlinearity, which could be desired for modulation, and suffers from nonlinear absorptions when its third-order optical nonlinearity is exploited [7]. Furthermore, silicon response is volatile, thus it is not appropriate for applications where the power consuming is critical or where data storage is needed, such as optical memories.

In spite of the issues mentioned before, there are some research articles describing the design process to achieve light emission by using third harmonic generation [8], but it is not well-proved in practical environments.

Table 1 lists the advantages and disadvantages mentioned in this introduction. Considering all of them, silicon photonics is a quite powerful platform that will be crucial in future telecommunication systems.

Advantages	Drawbacks
CMOS compatibility	Light generation
High refractive index contrast	Electro-optic effect
Transparent to light in telecommunication wavelengths	Difficult coupling to fibres
Low cost	Volatile response

Table 1. Advantages and disadvantages of silicon photonics platform.

I.2 Introduction to GST and its properties

I.2.1 Phase Change Materials

Devices based on phase change materials (PCMs) have emerged for on-chip switching and routing [9]. The reason is that the phase transition in PCMs generates huge optical property modulation (e.g., index change >1) that allows compact device architectures. Furthermore, such phase change can be either volatile [10] or non-volatile [11], enabling a large number of different applications.

Materials such as vanadium dioxide (VO_2), which exhibits a large change of refractive index at telecommunication wavelengths between its insulating and metallic state, are being used to develop optical modulators [12][13], switches [14] or photodetectors [15]. Another promising group of PCMs are chalcogenides, such as germanium-antimony-tellurides. By using $\text{Ge}_2\text{Sb}_2\text{Se}_4\text{Te}_1$ (GSST) or $\text{Ge}_2\text{Sb}_2\text{Te}_5$ (GST) as active material, research groups are creating phase-change memories [16][17][18] taking advantage of the non-volatile behaviour of these materials.

I.2.2 GST

GST is a chalcogenide that presents two states, amorphous (aGST) and crystalline (cGST). Changing between them can be triggered either optically or electrically. Usually, the material is in amorphous mode when fabricated, thus it is necessary to elevate its temperature to $\sim 250^\circ\text{C}$ to change the state into crystalline. Once the change is produced, GST remains crystalline (non-volatile) until the amorphization conditions are suited. These conditions are not only heating the material up to $\sim 650^\circ\text{C}$ but also a fast cooling ($>1^\circ\text{C/ns}$) to avoid the possibility of recrystallization. The process involved is denominated melt-quench.

The refractive index of GST, in both real and imaginary components, is wavelength dependent, as depicted in Fig. 2. For telecommunication wavelengths in second optical window (O-band, centred in 1310 nm) or third window (C-band, centred in 1550 nm), the difference between amorphous and crystalline in n and k is remarkable. This singular attribute permits the development of ultra-compact and high-performance optical switches based on hybrid structures, where GST is the active material.

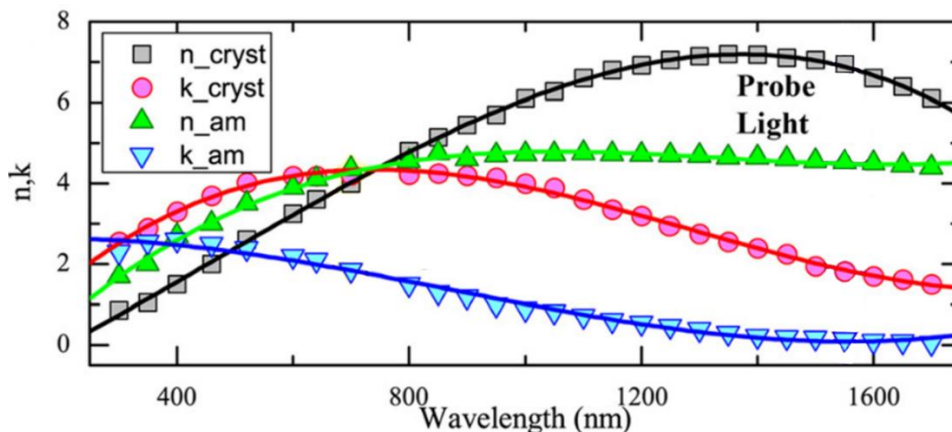


Fig. 2. Refractive index of GST in dependence of wavelength [17].

I.3 Review of the state of the art of devices based on Si/GST technology. Functionalities and possible applications

The $\text{Ge}_2\text{Sb}_2\text{Te}_5$ is a well-known PCM material, thus it is widely used in combination with silicon due to the interesting capabilities that have both materials together. The most important features are related with switching applications and optical memories. Just as reprogrammable circuits are very interesting in electronics, they are also attractive in photonics. Therefore, much of the effort in developing Si/GST technology are about designing reprogrammable devices to carry out the same tasks that nowadays are made with electronics.

As an example, in [19] a reconfigurable PIC platform is discussed, achieving energy efficiency and non-volatile behaviour in a compact device. One interesting point in their work is that they cover the GST layer with an indium tin oxide (ITO) thin film of 11 nm to protect the GST from oxidation. Some other similar research have been made that offer a promising solution for applications like large-scale rewritable optical circuits [20]. On the other hand, a 1x2 optical switch is demonstrated in Fig. 3 by using a grating-assisted contra-directional coupler [21].

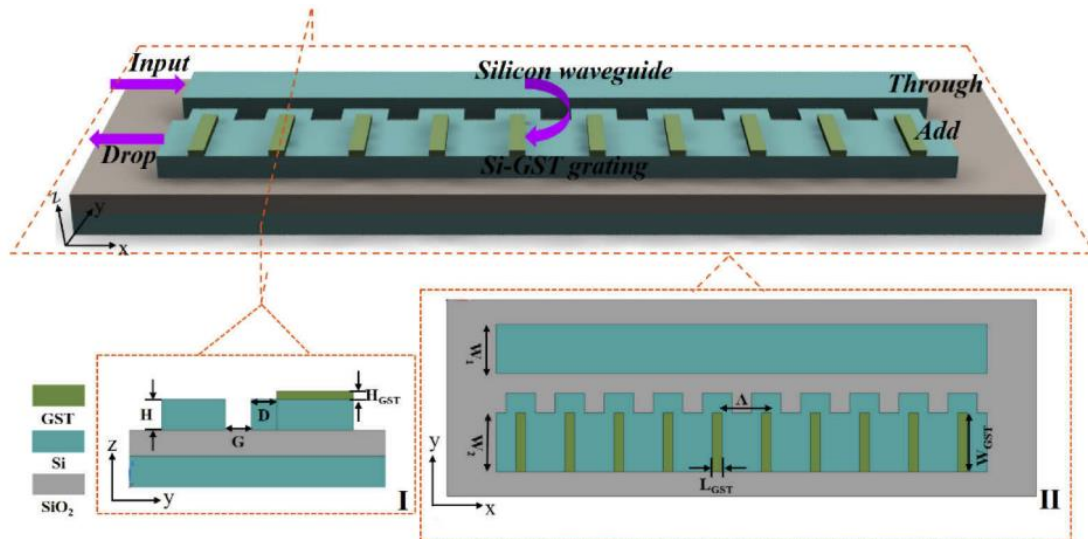


Fig. 3. 3D view of the contra-directional coupler enabled by Si/GST grating. I is the cross-sectional view of the coupler. II shows the top view. [21]

Modulators are another possible application of Si/GST technology, as it is shown in Fig. 4 [22]. They propose an electro-optical modulator integrated with phase change material GST, incorporating a hybrid Si-GST-Cu waveguide with Si waveguides in the input and the output. Extinction ratios above 5.4 dB are demonstrated on C-band (1530 nm to 1565 nm) using an active segment of $0.2 \mu\text{m}^2$. Moreover, energy consumption per bit for this nano-size device is on the order of nJ or sub-nJ per cycle.

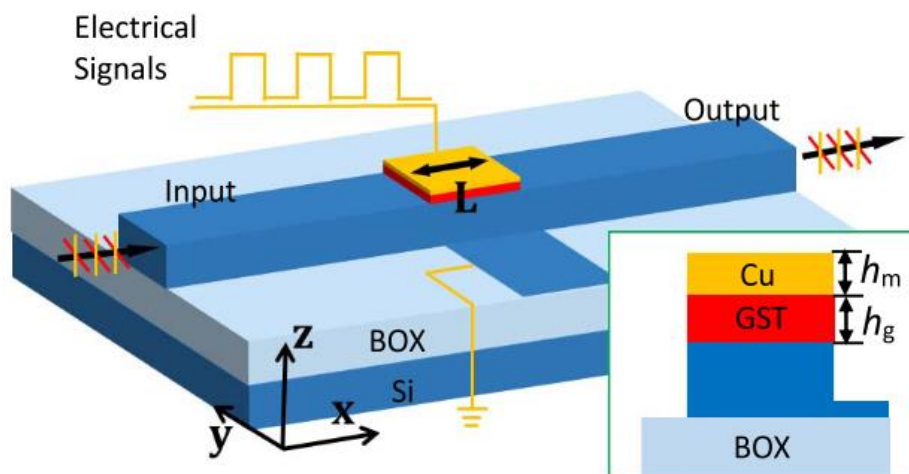


Fig. 4. Hybrid Si-GST-Cu waveguide modulator [22].

Apart from the previous applications, GST is also used for some stunning purposes, such as neuromorphic computing. Two examples of this topic are the articles published in Science on 2017 [23] and 2018 [24], which demonstrate the relevance of PCMs in different fields. Moreover, there is other interesting article that reports a tunable biosensor for the detection of biomolecules using GST [25]. Phase change property of the PCM allows tunable biosensing application, thus

they have tested on different concentrations of biomolecules, such as hemoglobin (10 g/l, 20 g/l, 30 g/l and 40 g/l) and urine (0–1.5 mg/dL, 2.5 mg/dL, 5 mg/dL and 10 mg/dL). The structure created to measure the biomaterials is as simple as the device shown in Fig. 5.

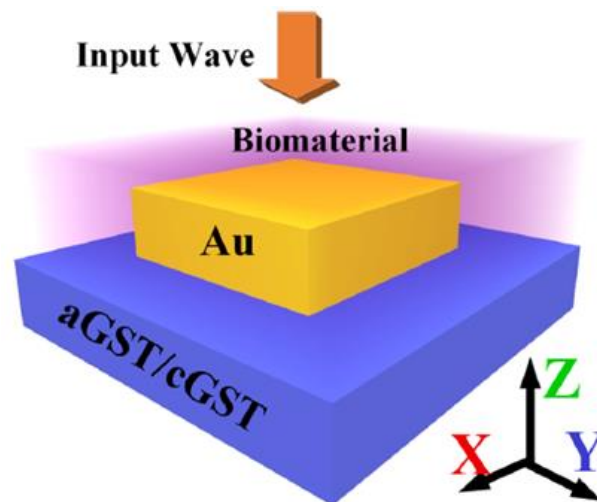


Fig. 5. 3D view of the biomolecular photonic sensor [25].

All in all, the main advantage of phase change materials and, specifically, GST, is the opportunity to create reconfigurable devices. By using this property, it is possible to create optical field-programmable gate arrays (Optical FPGAs), which are commonly used in digital signal processing (DSP), software defined radio (SDR) systems, ASIC prototyping, medical imaging systems, computer vision systems, among other applications. Therefore, PCMs can improve speed, reduce footprints or increase bandwidth in this kind of devices.

II. Objectives and methodology

II.1 Objectives

The main objective of this work is design, analyse and demonstrate experimentally the behaviour of GST phase change material, combined with silicon, to develop applications that required non-volatile switching. In particular, GST characterisation in terms of propagation losses and phase shift produced when changing states is analysed in depth.

To analyse the response of the GST, hybrid Si/GST waveguides and ring resonators have been simulated, fabricated and measured.

The following specific objectives have been set to accomplish the mentioned above:

- Analysis of GST optimal thickness.
- Design and analysis of hybrid Si/GST propagation losses by using straight waveguides.
- Design and analysis of hybrid Si/GST phase shift on optical ring resonators.
- Characterisation of experimental samples and validation of designs.
- Final discussion about the obtained results and proposal of future work.

II.2 Methodology

In order to fulfil the objectives mentioned above, the methodology presented in Fig. 6 has been followed. After the initial section of documentation to get familiar with the technology, some preliminary simulations were carried out to test the predicted behaviour of the component. Then, after the fabrication of the device, the gross of the work was related to characterisation. Characterisation includes preparing the required setup, doing the measurements and analyse the results. Thus, this work involves a high workload in terms of measurements and data processing.

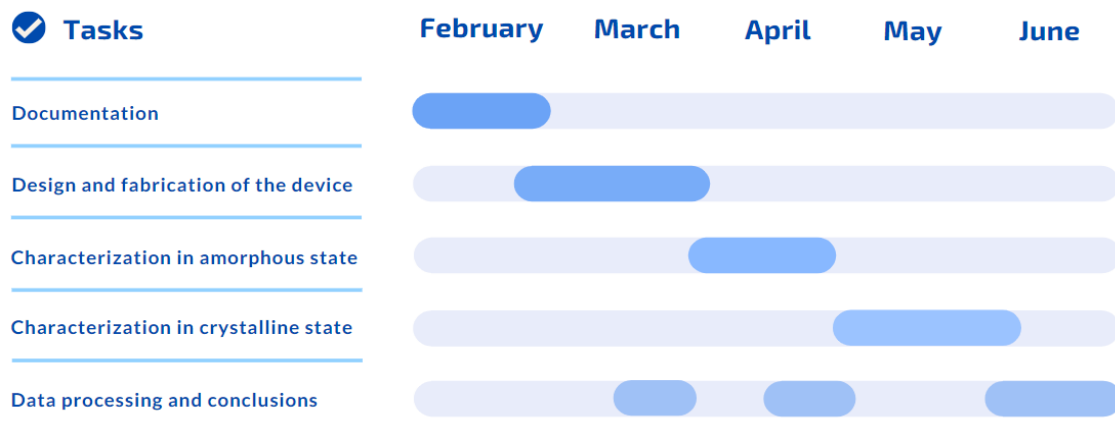


Fig. 6. Time diagram of the tasks developed.

This work was carried out in the Nanophotonics Technology Center (NTC) of Valencia, and it was supervised by Prof. Pablo Sanchis Kilders¹ and PhD candidate Jorge Parra Gómez.

The software programs employed to simulate the structures are FemSIM, which is a mode solver based on Finite Element Method (FEM), and FullWAVE, based on Finite-Difference Time-Domain (FDTD) method. Both programs are integrated in the RSoft CAD Environment from Synopsys². On the other hand, the program used to process the data acquired with the measurement equipment is MATLAB.

¹ Head of Photonics Integrated Devices research line. <http://orcid.org/0000-0003-2984-4218>

² <https://www.synopsys.com/photonic-solutions/rsoft-photonic-device-tools/cad-environment.html>

III. Design of Si/GST hybrid waveguides and switching techniques

III.1 Design of Si/GST hybrid waveguides

Waveguides are the most basic building block in every photonic circuit, thus it is vital to demonstrate the performance of the GST in these kind of structures. Hybrid Si/GST waveguides, where the active material is on top, are the best option to evaluate the properties of the material. In this work the technology used is SOI, where the thickness employed is 220 nm for the Si layer and 2 μm for the SiO_2 substrate.

Determining the thickness of the GST layer is crucial. Thicker layers can produce higher-order modes in the hybrid structure and, therefore, an unexpected behaviour of the switching performance [26]. Therefore, an optimal value to avoid the coupling of higher-order modes must be determined. The optimization of the thickness was performed by simulating the structure shown in Fig. 7 using FemSIM and FullWAVE (3D-FDTD), in which the length of the GST was chosen according to the size of the circuits to be created. The results of the simulation are shown in Fig. 8.

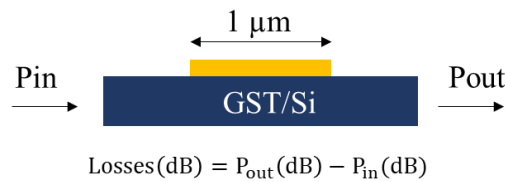


Fig. 7. Simulated hybrid Si/GST waveguide.

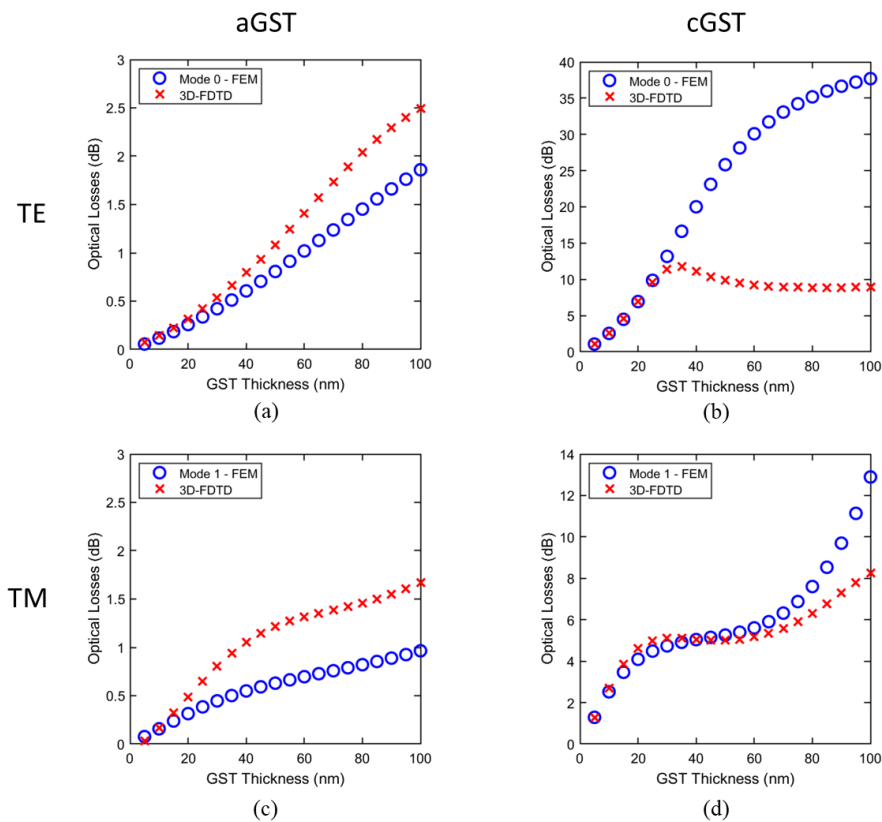


Fig. 8. Comparison of optical losses computed with FemSIM and 3D-FDTD. (a) TE aGST. (b) TE cGST. (c) TM aGST. (d) TM cGST.

Considering the graphs in Fig. 8, a divergence between what is simulated with FemSIM and 3D-FDTD is seen when the thickness of the GST layer increases. This divergence is clearly accentuated from 30 nm onwards for the crystalline state in TE polarization, thus it is considered as the most restrictive situation. It is remarkable that single-mode condition may not be met, but achieving the closest single-mode behaviour in both polarizations is the goal of the design. All in all, there is a trade-off between achieving the best optical performance while avoiding excitation of higher-order modes. Defining the figure of merit shown in equation (1) and plotting the simulation results for TE polarization (Fig. 9), it is possible to conclude that the optimal thickness must be lower than 30 nm.

$$FOM = \frac{ER}{IL} \quad (1)$$

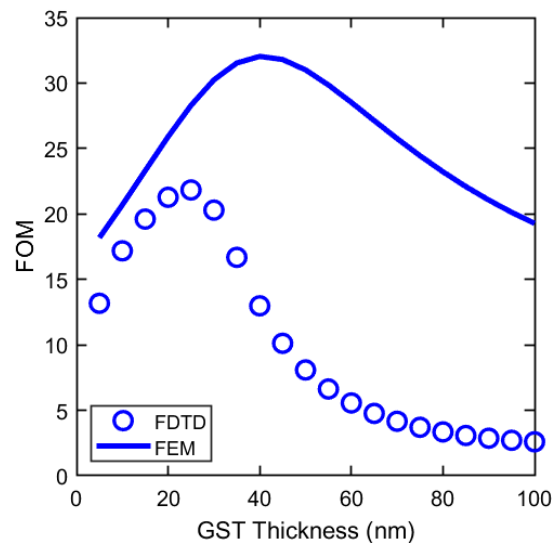


Fig. 9. Results of the figure of merit defined by equation(1) for TE polarization.

Finally, the thickness chosen for the GST layer is 25 nm, as depicted in Fig. 10. A standard silicon waveguide (500-nm-wide and 220-nm-thick) has been employed, whereas different lengths of the GST patch have been considered.

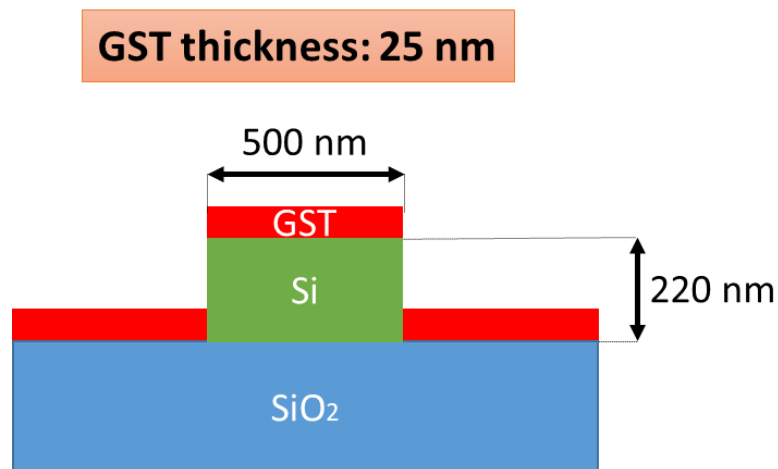


Fig. 10. Cross-cutting of the Si/GST waveguide.

Propagation losses and phase shift of the hybrid GST/Si waveguide are the main parameters to be considered in the design stage. Propagation losses (α [dB/ μ m]) are defined by equation (2), while the propagation constant, or phase shift per unit length (ϕ/z [rad/ μ m]), is described by equation (3).

$$\alpha = \frac{20 \log_{10}(e) 2\pi}{\lambda} \text{Im}(n_{\text{eff}}) \quad (2)$$

$$\beta = \frac{\phi}{z} = \frac{2\pi}{\lambda} \text{Re}(n_{\text{eff}}) \quad (3)$$

Both losses and phase shift variation are polarization dependent, thus it is necessary to calculate them for TE and TM. Before computing the required values, the effective index of the hybrid waveguide must be simulated, as it is shown in Fig. 11. For these simulations, the refractive index of GST was estimated from Fourier-Transform Infrared (FTIR) spectroscopy measurements, obtaining the indices for the amorphous and crystalline states: $n_{\text{GST-A}} = 3.798 + 0.074j$, $n_{\text{GST-C}} = 6.462 + 1.074j$.

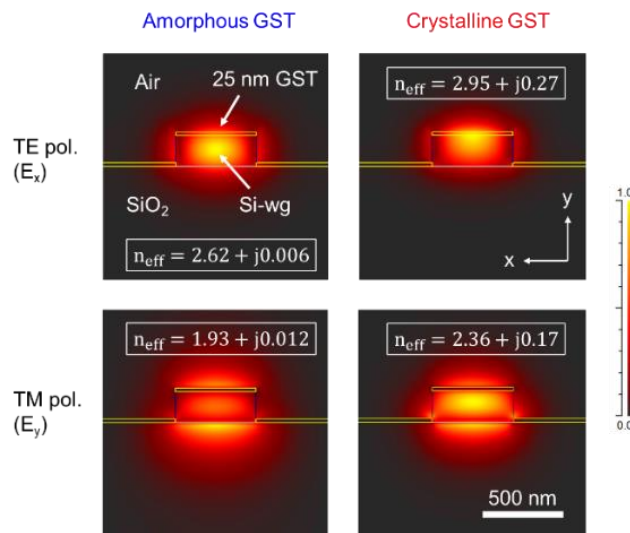


Fig. 11. Simulation of hybrid GST/Si waveguides in TE and TM.

By using the n_{eff} shown before and substituting in the equation (2), the propagation losses of each polarization for amorphous (A) and crystalline (C) were calculated, and they are presented in Table 2.

Polarization	α_A (dB/ μ m)	α_C (dB/ μ m)
TE	0.212	9.506
TM	0.422	5.985

Table 2. Propagation losses of hybrid GST/Si waveguide in TE and TM.

On the other hand, by using the equation (3), the values of phase shift variation in amorphous and crystalline have been obtained, as it is shown in Table 3.

Polarization	β_A (rad/ μ m)	β_C (rad/ μ m)
TE	10.62	11.96
TM	7.82	9.57

Table 3. Phase shift variation of hybrid GST/Si waveguide in TE and TM.

III.2 Design and simulation of validation photonic structures

III.2.1 Structures to determine the propagation losses: straight hybrid waveguides

Analysing the propagation losses of GST requires the use of different patch lengths in amorphous and crystalline states. By following the simulation results presented in Fig. 11 and the estimated propagation losses in Table 2, patch lengths were defined in TE and TM. These patches will be located on a standard straight silicon waveguide connected to grating couplers for fiber-to-chip coupling (input and output), thus it is the simplest structure. Furthermore, between the grating couplers and the 500-nm-wide waveguide, it is necessary to add tapers, as it is shown in Fig. 12.



Fig. 12. Example of a straight silicon waveguide for propagation losses estimation.

Propagation losses will be estimated by measuring a set of identical waveguides with different GST patch lengths, as listed in Table 4. As the absorption is much higher in crystalline state than amorphous state, lengths to analyse the properties of GST must be largely different. In the design there are two columns: left column (cGST) contains shorter GST strips, which will be used to measure the propagation losses in crystalline state, and right column (aGST), where the GST patches are longer, in order to evaluate the performance when the material is in amorphous state.

Polarization	Length (μm) aGST	Length (μm) cGST
TE	0-4 (step 0.5)	0-14 (step 2)
TM	0-120 (step 15)	0-140 (step 20)

Table 4. Parameters for straight waveguides.

The remaining structures in the Fig. 12 are tapers and gratings. Starting from the gratings, they are designed for working at 1550 nm, and optimized for a SiO_2 cladding. Therefore, since the SiO_2 cladding was not deposited yet, the response of the gratings has moved slightly. This fact must be considered even though it does not affect the final results. The other structures, tapers, are needed to connect gratings to the standard silicon waveguide. The chosen size is due to how it will be measured in the characterisation setup, which will be shown in the experimental results section.

The parameters of the gratings employed are listed in Table 5, whereas the length of the tapers is 200 μm .

Polarization	Pitch (nm)	Fill factor	Etched Si (nm)
TE	630	0.388	70
TM	1000	0.43	70

Table 5. Parameters of gratings for TE and TM.

III.2.2 Structures to analyse the phase shift variation: optical ring resonators

Phase shift variation is the second parameter to analyse, thus a structure to estimate such phase shift in an easy way is desirable. The use of a Mach-Zehnder Interferometer (MZI) is a possibility because its performance depends on the relative phase shift variations between two optical signals derived by splitting light from a single source. However, a resonating structure has been selected, the ring resonator because it is more sensitive to refractive index variations. This kind of structure

consists of a waveguide in a close loop coupled to another waveguide, as it is shown in Fig. 13. The structure will be resonant for light which after each full trip around the ring constructively interferes with the input light. Optical intensity in the ring is built up and hence significantly increased.

The ring resonator shown below has a parallel section between the ring and the signal waveguide, thus it is called racetrack ring resonator. This means that there is a parameter called coupling length (L_C) that can be modified to obtain the desired performance in terms of extinction ratio. On the parallel region, the structure works as a directional coupler. The coupling coefficient (K) depends both on the gap (d) and the coupling length. As the gap will be a fixed value due to fabrication constraints (300 nm), the parameter that will change to obtain the desired behaviour is the coupling length.

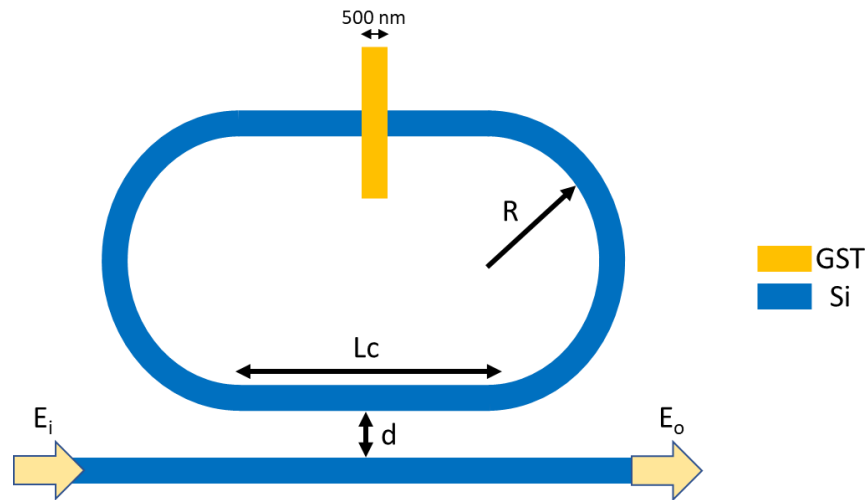


Fig. 13. Optical ring resonator with a hybrid GST waveguide.

The following parameters of the rings were designed to evaluate the phase shift variation [26]. These parameters are the radius (R) and the coupling length (L_C), apart from the length of the GST strip. The design strategy is varying L_C in order to find a region with large extinction ratio (close to the critical coupling). The expected value can move due to fabrication tolerances and small variations in the refractive index of GST, thus it is necessary to define a range of L_C where the desired performance will be located. Then, considering the predicted phase shift calculated in Table 3, the length of the GST patch was defined. The chosen value should ensure low loss and give rise a perceptible phase shift while being able to determine the resonances of the ring with the GST in both states, as it is discussed on the following. Therefore, a phase variation of $\pi/4$ was considered as appropriate, for which a 500-nm-long strip is required.

As it was previously mentioned, the coupling length and K are dependent. In order to select the range of values of L_C for TE and TM polarization, a simulation of the response of the coupling coefficients in aGST and cGST for both polarizations was done. Firstly, considering losses in silicon as negligible, the extinction ratio was calculated by the equations below, where $t = \sqrt{1 - K}$ and a is the optical loss induced by the GST layer, which is estimated with the values of the propagation losses and the length of the GST strip (different values for amorphous and crystalline states).

$$ER = \frac{Tt}{Rmin} \quad (4)$$

$$Tt = \frac{(t + a)^2}{(1 + t \cdot a)^2} \quad (5)$$

$$R_{min} = \frac{(t - a)^2}{(1 - t \cdot a)^2} \quad (6)$$

By using the values of the propagation losses of Table 2 and considering 1dB additional loss due to the propagation losses in the silicon waveguide without GST, the results shown in Fig. 14 were obtained. Notice that the maximum extinction ratio (critical coupling) is achieved when the output power at resonance is zero, thus the optimal coupling coefficient for amorphous and crystalline is different.

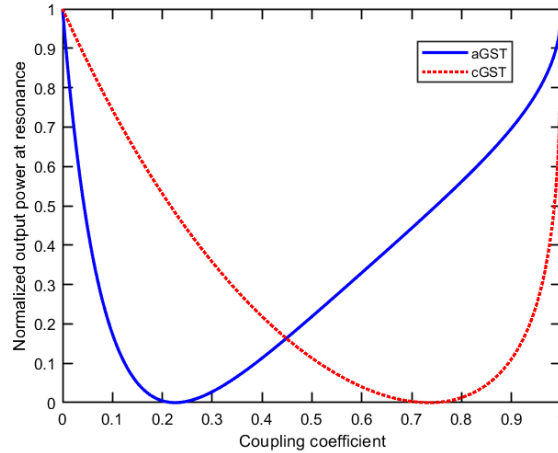


Fig. 14. Normalized output power at resonance vs. the coupling coefficient (K) for TE polarization.

The response of the ring resonators with the hybrid Si/GST structure for different coupling values is analysed in Fig. 15. To perform these simulations, the effective indices of the structures in TE and TM polarization were computed with FemSIM. Fig. 15(a) corresponds to the simulation for the optimal coupling coefficient for GST in amorphous state. This means that the normalized output power at resonance is ideally zero ($-\infty$ in dB). Meanwhile, in crystalline the resonance peak has only around 5 dB of extinction ratio, as could be seen from the graph of Fig. 14. Fig. 15(b) is the opposite case, where the optimal coupling coefficient for crystalline GST was chosen. On the other hand, Fig. 15(c) depicts an intermediate value close to the point where both coupling lines intersect. By using this value is possible to evaluate the phase shift of the resonances in aGST and cGST.

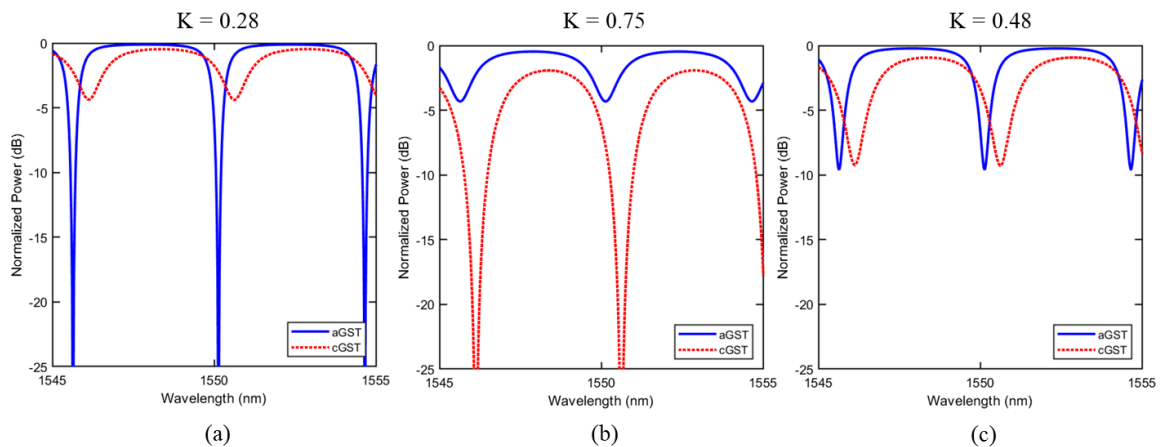


Fig. 15. Response of a ring resonator in TE polarization for different coupling coefficients. (a) Maximizing the ER in amorphous (K = 0.28). (b) Maximizing the ER in crystalline (K = 0.75). (c) Intermediate value of the coupling coefficient to analyse the phase shift.

Analogously for TM polarization there are two different values that optimize the extinction ratio, as it is shown in Fig. 16. It is interesting that the optimal value in amorphous is very similar, while the corresponding K for crystalline has changed more. This is the expected behaviour because the differences between the propagation losses for TE and TM are much higher for cGST than aGST.

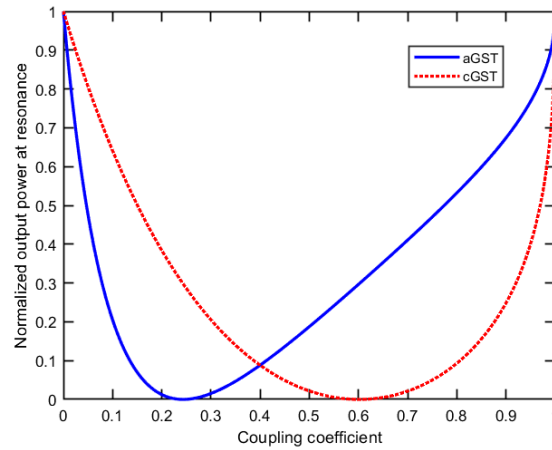


Fig. 16. Normalized output power at resonance vs. the coupling coefficient (K) for TM polarization.

Fig. 17 shows the simulation of the ring response in TM polarization. Fig. 17(a) and Fig. 17(b) show the results for the optimal values of coupling coefficient, where Fig. 17(c) depicts a simulation for an intermediate value of K .

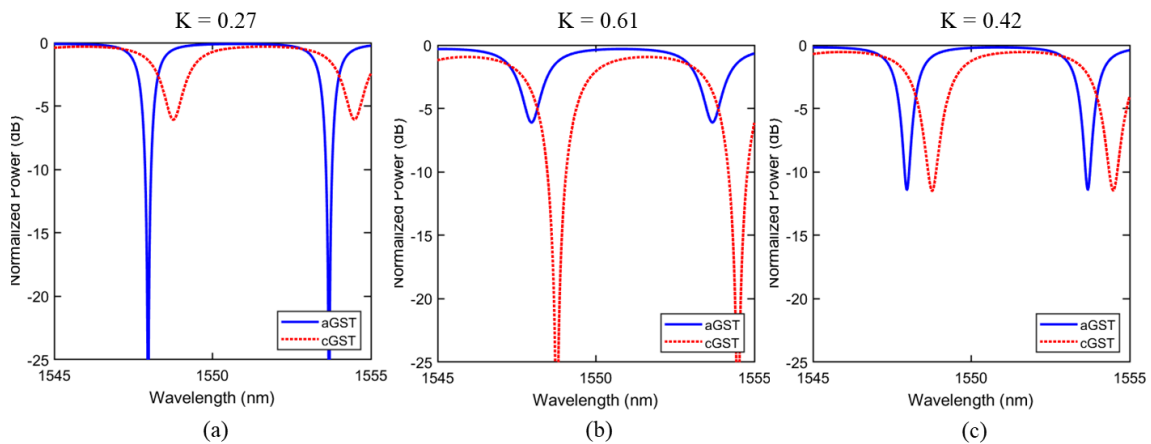


Fig. 17. Response of a ring resonator in TM polarization for different coupling coefficients. (a) Maximizing the ER in amorphous ($K = 0.27$). (b) Maximizing the ER in crystalline ($K = 0.42$). (c) Intermediate value of the coupling coefficient to analyse the phase shift.

Considering those issues, the parameters chosen for the racetrack ring resonators are shown in Table 6. The radius was selected to neglect bending losses, while the coupling lengths were chosen to cover a wide range of the coupling coefficient values in order to obtain measurable extinction ratios for the GST in amorphous and crystalline states.

Polarization	$R(\mu\text{m})$	$L_c(\mu\text{m})$
TE	5	40-85 (step 5)
TM	15	7-16 (step 1)

Table 6. Parameters for ring resonators.

III.3 Review of switching techniques

Switching in phase change materials can be triggered by injecting an optical pulse or electrically. In this section, different switching techniques are reviewed and discussed.

III.3.1 Electrical switching

Electrical switching is the oldest method between optical and electrical. It also has some parallels in other technologies, such as transistors or memristors. To produce the switching of the GST through electrical signals there are two different methods. On the one hand, it is possible to use an electrical current for achieving the phase change by following the same principle of memristors [27]. On the other hand, using an external electrical circuit connected to a heating element is also possible. In this scheme, the heat is generated due to the resistance to electric current of the materials. The most commonly used are ITO heaters [28][29], PIN diode heaters [20][30], silver heaters [31] or the combination of more than one metal (Ti, AlCu) [32]. One example of switching using this technique is shown in Fig. 18.

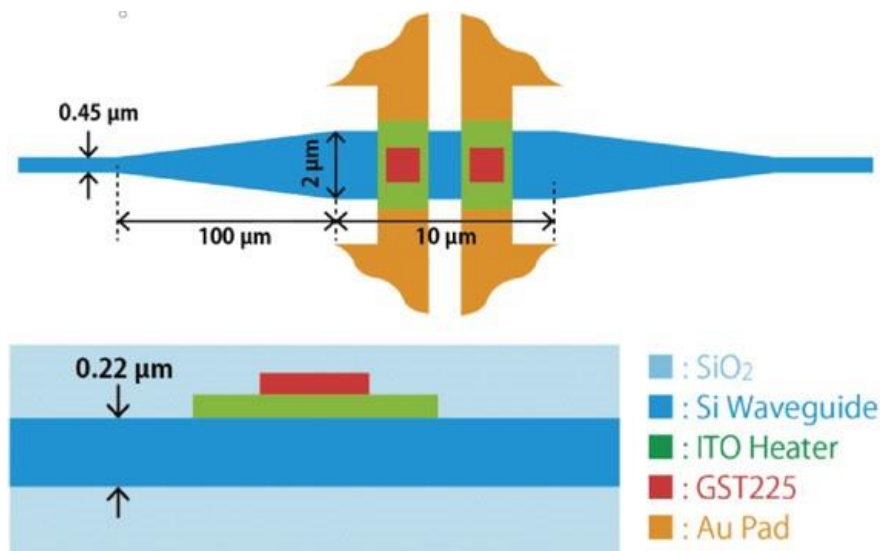


Fig. 18. Current-driven phase-change optical gate switch using ITO heaters [28].

Electrical methods have some advantages that must be considered. Firstly, the optical circuit and the heating circuit are separated and independent between them, therefore, the device is more controllable, and it is easier to have access to the optical circuits if necessary. Furthermore, the control electronics can be monolithically integrated due to the CMOS compatibility.

However, using this technique have some drawbacks. The main problem is the difficulty of generating a localized heating on the GST layer and satisfy the fast-cooling requirement for the amorphization process. On the other hand, it should be noticed that introducing these elements increases the number of steps of fabrication.

III.3.2 All-optical switching

All-optical switching uses an optical signal to produce the phase change in GST. In this situation, the heat required is generated by a high-energy laser pulse due to the photo-thermal effect, leading to switching in the GST. This change can be achieved in two different ways. First of them is using an external laser, which impacts on the material from the far-field and excites it to achieve the switching [19][33]. This method is denominated out-of-plane all-optical switching and it is the principle used in [34] or [35], where a gate switch using GST as active material is demonstrated. Another example of this method is shown in Fig. 19, which consists of a device for optical switching at 1550 nm in silicon racetrack resonators [36]. Fig. 19(a) presents the structure with

the rings, where the left one contains an overcladding layer of GST, whereas the right ring is free of GST. Fig. 19(b) is the schematic of the experimental setup for device characterisation, where it is possible to see the perpendicular optical pulse injected to the GST by using a lens to focus the beam.

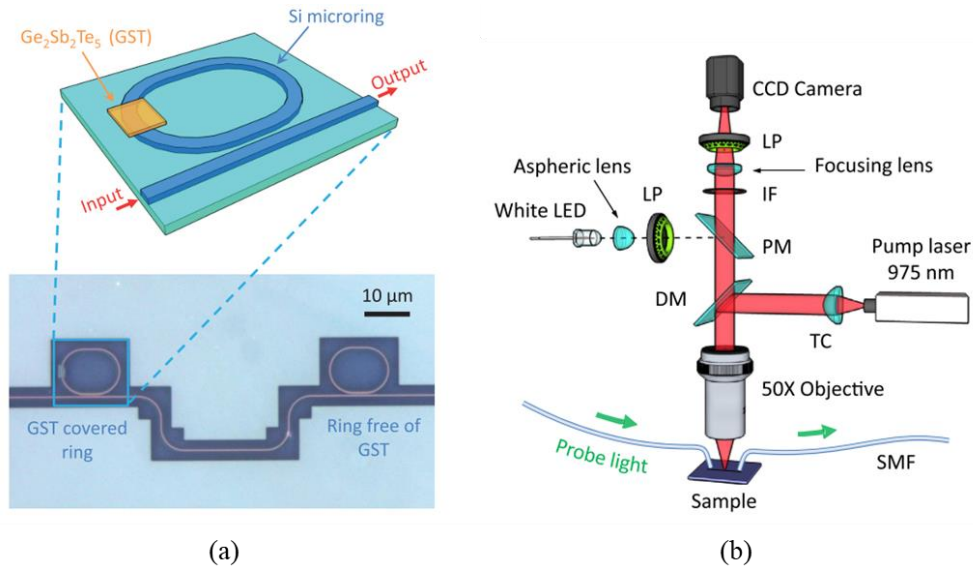


Fig. 19. Device for optical switching at 1550 nm in silicon racetrack resonators [36]. (a) Structure with ring resonators. One of them (left) contains an overcladding layer of GST. (b) Schematic of the experimental setup.

The second method is known as in-plane all-optical switching, and it is used for on-chip devices. This method involves evanescent field coupling, where a control signal from high-powered laser traverses through the on-chip waveguide in order to achieve a phase switch in the material [37][38]. A good example of the method mentioned before is shown in Fig. 20 [39]. Signal beam and control beam are guided in the same waveguide structure. By injecting an ultra-short optical pulse, it is possible to change the behaviour of the GST layer between amorphous and crystalline.

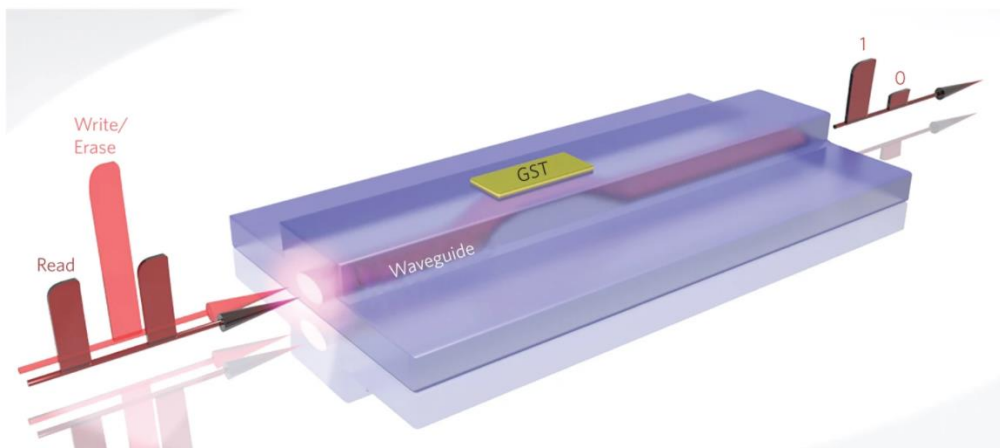


Fig. 20. Structure of an all-optical on-chip memory cell [39].

Evanescent coupling is advantageous due to the large absorption coefficient in most of the used PCMs. The in-plane deployed GST increases the interaction between the material and the optical wave, leading to smaller footprints.



III.3.3 Comparison between optical and electrical switching

To sum up, optical switching seems to be better in terms of speed and energy efficiency based on results reported in the literature. Switching using pulsed lasers with low-power consumption has been reported, which is a promising result for energy efficiency schemes. Moreover, using the same optical circuit, the size of the device is less bulky. However, the design and fabrication are more complex and sometimes it is not possible to access the material individually, which could be necessary for some applications.

On the other hand, electrical switching is better for large-scale integration systems. Furthermore, the photonic circuit is usually more complex than the electrical circuit. This fact, combined with the maturity of electronic devices, makes electrical switching convenient for some systems.

All things considered, each technique can be useful depending on the requirements.

IV. Experimental results

IV.1 Design of GDS and description of fabrication process

IV.1.1 Design of GDS

Graphic Design System file (GDS) is a design file created by different CAD applications that contains information about the design, layers, shapes and text labels. Nowadays, GDSII format is the *de facto* industry standard for data exchange of integrated circuits or IC layout artwork. There are several programs to create GDS. In fact, lithography equipment usually has their own software to perform this task. However, the program chosen in this project is KLayout, a widely used free software to view and create GDS files.

KLayout permits the creation of polygons, curves or circles, thus drawing the structures directly using the software as a possibility. Nevertheless, a MATLAB library to design the structures as building blocks has been made by our team, where the desired structure can be created by entering the parameters shown in Fig. 21 and Fig. 22. Then, it is only necessary to instantiate them in KLayout.

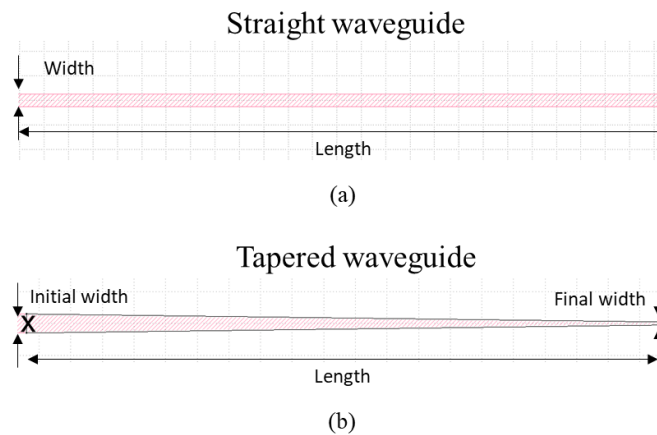


Fig. 21. Parameters of building blocks to create GDS. (a) Straight waveguide. (b) Tapered waveguide.

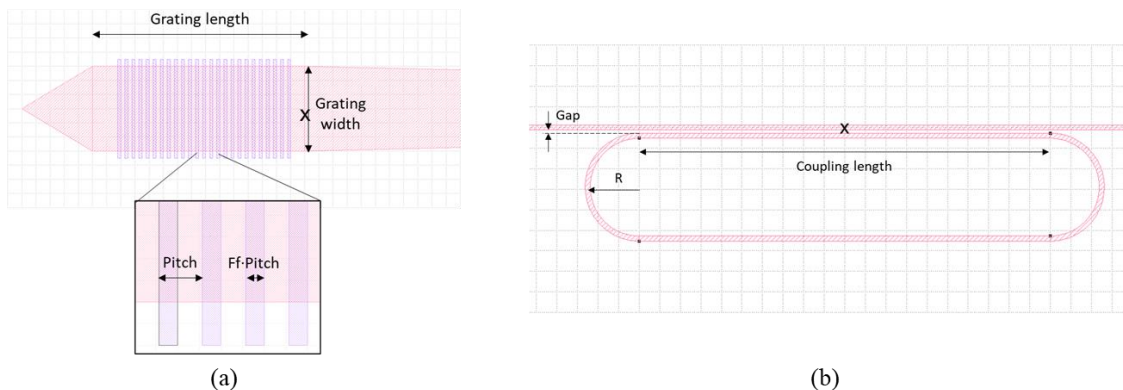


Fig. 22. Parameters of building to create GDS. (a) Linear grating coupler. (b) Ring resonator.

All the values needed to determine the parameters of the previous building blocks were presented in section III.2: Design and simulation of validation photonic structures. With them, and using the method described above, the GDS structure depicted in Fig. 23 was created. In the picture, the waveguides and rings (silicon) are represented in pink, while the gratings are light purple-coloured and the GST patches are blue-coloured.

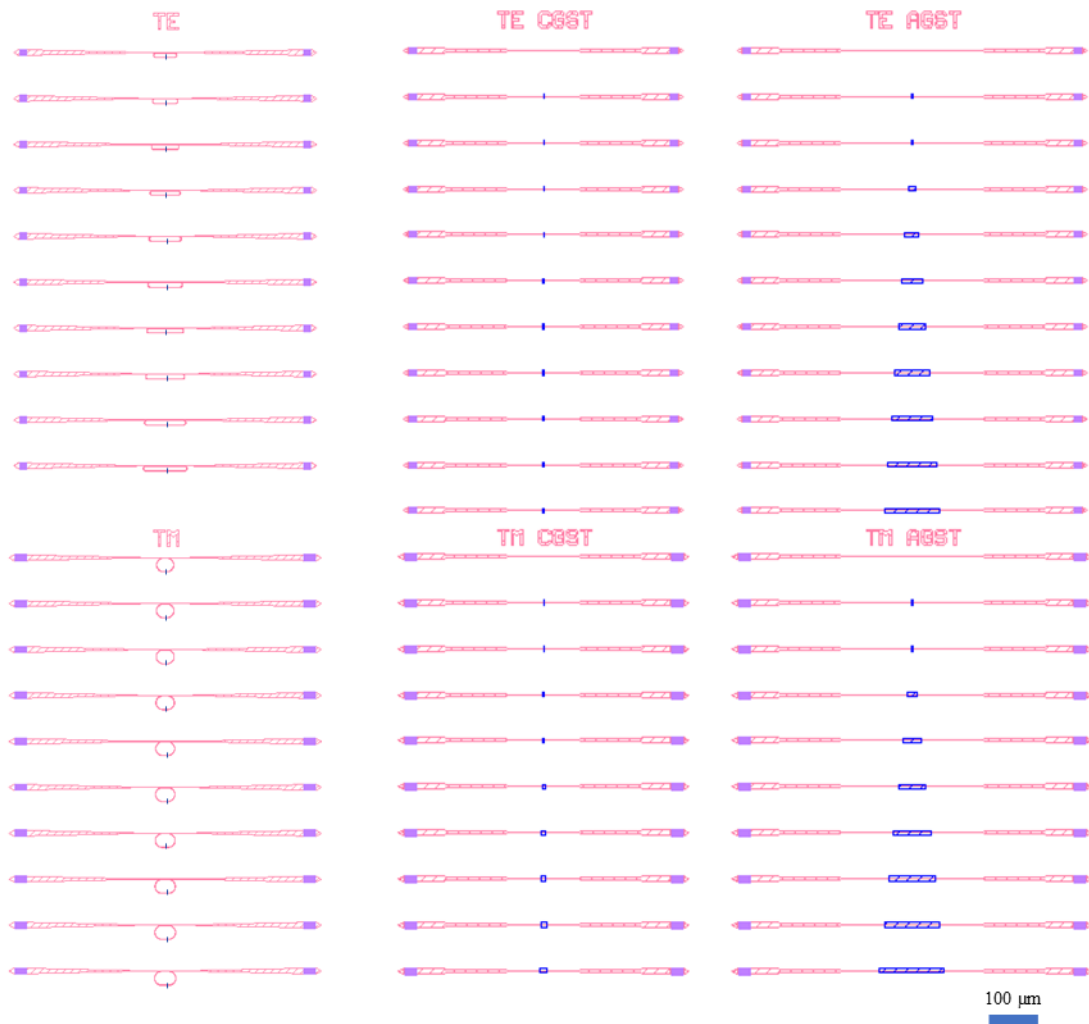


Fig. 23. Screenshot from KLayout of the designed structure to export to GDS.

IV.1.2 Fabrication process

First, the sample was fabricated only with the silicon structures (waveguides, rings and gratings). To carry out this process, a top-down nanofabrication technique has been followed, represented by the diagram depicted in Fig. 24.

Starting from the chosen substrate, it is necessary to cover it with a resist in order to perform the lithography process. The lithography technique employed is called electron beam lithography (EBL or *e-beam*), where the used photoresist was PMMA, and the *e-beam* equipment was Raith 150. Two etching processes were required for the silicon structures. Firstly, a full etching process was employed for the waveguides. Secondly, shallow etching of 70 nm was performed to define the grating couplers. Finally, a lithography process was also used to define the GST patches. Afterwards, a 25-nm-thick GST layer was deposited by an evaporation process, followed by a lift-off technique.

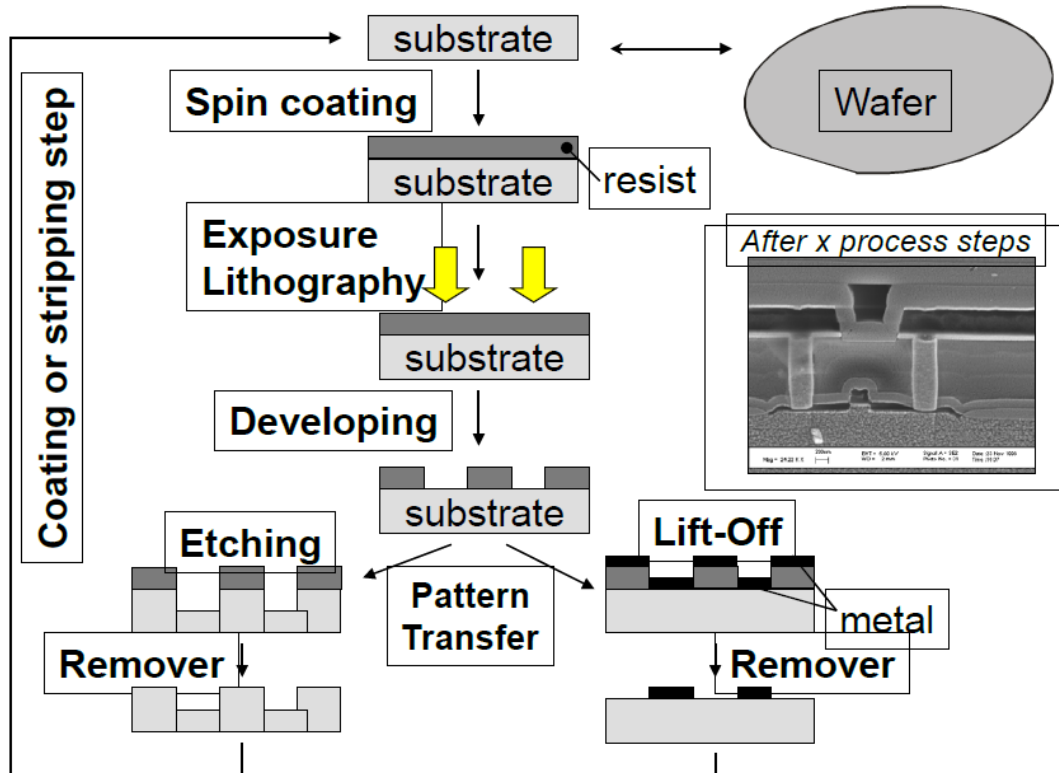


Fig. 24. Diagram of top-down nanofabrication process.

To sum up, the sample was firstly fabricated with only the silicon structures. Then, the 25-nm-thick layer of GST was fabricated in the areas indicated on the GDS file.

IV.1.3 Images of the fabricated sample and fabrication discrepancies

The images presented in Fig. 25 and Fig. 26 were obtained by Scanning Electron Microscope (SEM). At the top, two ring resonators are shown. Fig. 25(a) is TE polarization and Fig. 25(b) is TM polarization. Meanwhile, the lower part shows the coupling region of one of the rings. Here it can be seen that the design values have slightly deviated in production. The waveguides, which were designed for a width of 500 nm, are now 570 nm wide, as depicted in Fig. 26(a). Consequently, the gap between the waveguides is 232 nm (compared to the 300 nm designed), as shown in Fig. 26(b). However, despite these deviations from the target design, the optical response of the waveguides should not be significantly altered, whereas possible variations of the coupling coefficient are covered by the wide range of coupling lengths used.

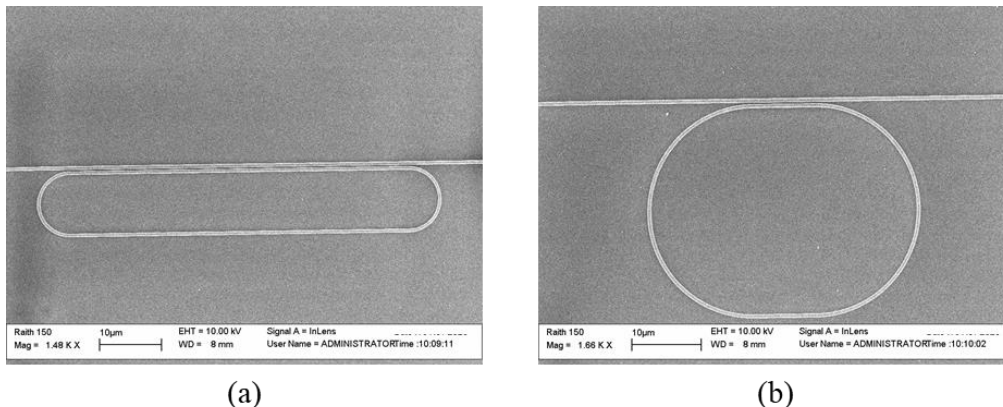


Fig. 25. SEM images of the fabricated sample. (a) TE polarization ring. (b) TM polarization ring.

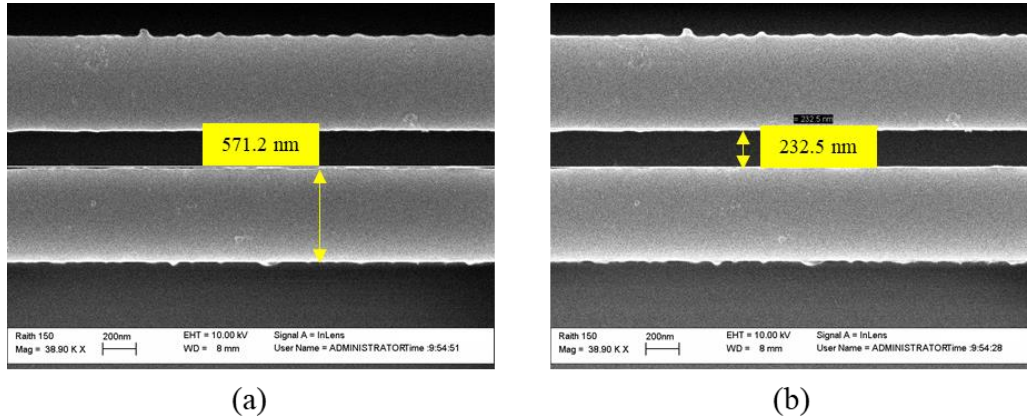


Fig. 26. Detailed view of the fabricated sample taken with SEM. (a) Width of the fabricated waveguides in a ring resonator. (b) Gap between waveguides in a ring resonator.

IV.2 Definition of characterisation process

IV.2.1 Characterisation of the sample: propagation losses and phase shift variation

Characterisation of the sample was carried out by using the elements shown in Fig. 27.

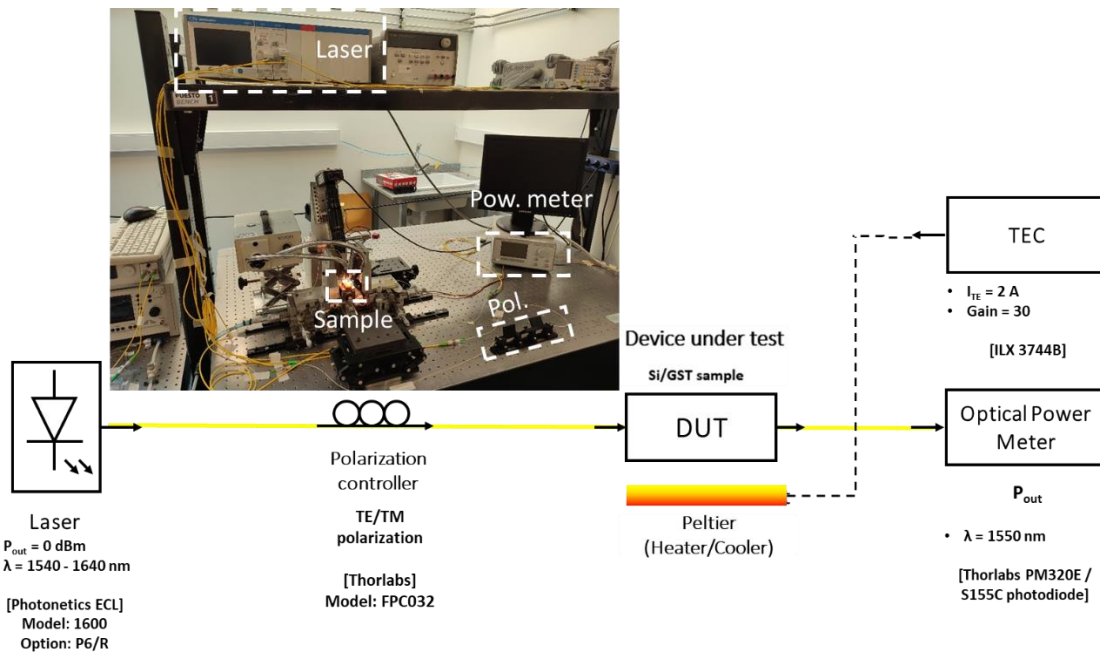


Fig. 27. Setup for characterisation of the sample. Top-left: real image. Bottom: schematic.

The laser employed allows to characterize the spectral response of the structures on a large bandwidth (from 1540 nm to 1640 nm). Then, a polarization controller is required after the light source. It must be adjusted when changing from TE and TM to achieve the highest output power, which is measured with the optical power meter (Thorlabs PM320E – S155C photodiode). Last element in the setup is the Peltier. As it is known, ring resonances are temperature sensitive, thus the Peltier is in charge of maintaining the temperature of the sample at a constant value (25 °C).

Controlling both laser and power meter is done with a computer by using a LabView program created by the NTC team. The software enables a wavelength sweep from 1540-1640nm, setting the step and the output power. Then, all the data is collected and exported to ASCII format files (e.g., .txt), which can be processed with MATLAB.

IV.2.2 Setup for all-optical switching

All-optical switching requires modifying the setup above by adding some other elements that has been specifically carried out for this work, as it is shown in Fig. 28. Firstly, an electro-optic (EO) modulator is incorporated after the polarization controller. This element is used to inject the ultra-short optical pulse (200 ns) depicted in Fig. 29, which leads the transition from crystalline to amorphous. EO modulator is DC biased with a power supply, whereas the pulse introduced to the device is created by using an arbitrary waveform generator (AWG). Then, to perform the switching, signal must be amplified. For that purpose, Amonics 30-B EDFA is chosen as the amplifier, which is followed by another polarization controller before reaching the device under test. Again, the temperature of the Si/GST chip is controlled by the Peltier. Finally, the signal is captured by using an optical power meter. Notice that, if the time response of the GST switching is desired, it would be necessary to use a digital communication analyser (DCA) or similar equipment to capture the changes in time domain.

It should be highlighted that optical switching in GST is different for aGST to cGST transition than the opposite. To crystallise the sample, other type of excitation is required (e.g., wider optical pulses or a pulse train).

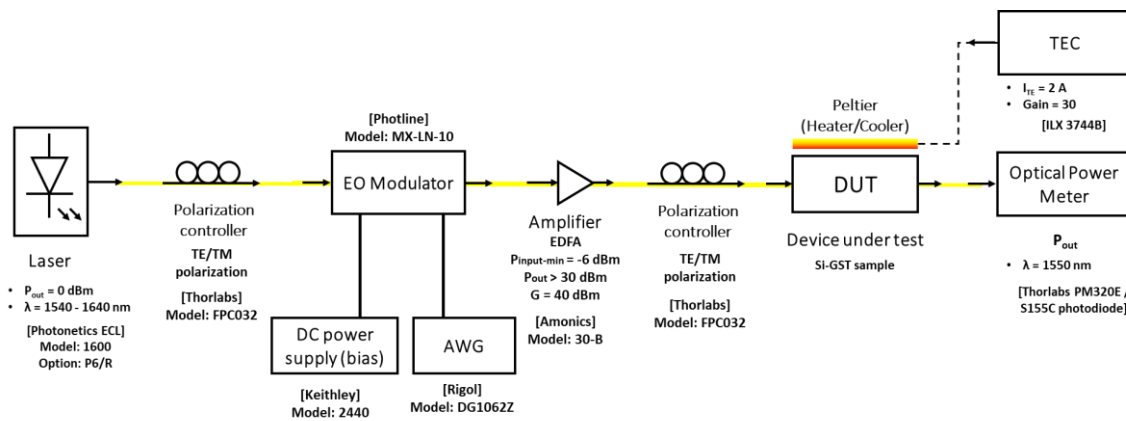


Fig. 28. Setup for all-optical switching.

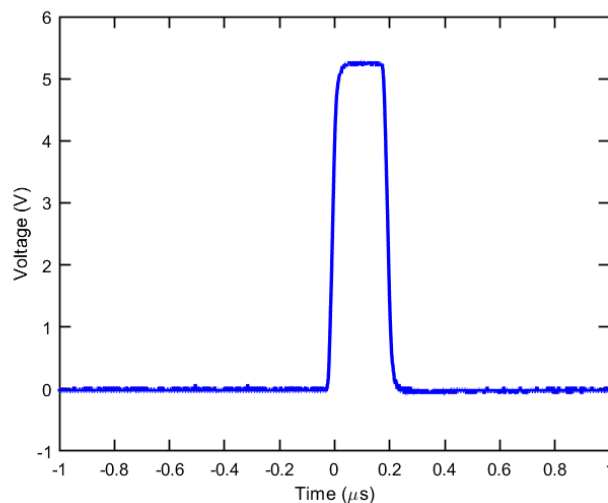


Fig. 29. 200-ns-wide electric pulse created with the AWG.

IV.3 Characterisation of absorption switching

IV.3.1 Images of the waveguides for propagation loss characterisation

Characterisation of propagation losses in the hybrid waveguides is discussed in this section. Firstly, before depositing the GST layer, all the waveguides were measured to check the behaviour was consistent with the design (i.e., attenuation is at the correct magnitude order). After checking that the initial state of the silicon waveguides and gratings were correct, the sample was handed over to the fabrication team to deposit the GST. Prior to GST deposition, the sample was cleaned using a piranha solution and oxygen plasma treatment.

In Fig. 30 it is possible to see the silicon waveguides fabricated after the GST deposition. Before doing any measurement, the sample was observed with the optical microscope in order to guarantee that GST deposition was done correctly. Despite the small dust particles in the chip that can be seen in Fig. 30(a) and Fig. 30(b), most of the structures present a good condition. However, Fig. 30(c) and Fig. 30(d) prove that the first waveguides designed to characterise the GST absorption in amorphous state (labelled in the sample as “TE aGST”) were damaged. This damage was produced between the preliminary measurements without GST and the deposition of the material. Unfortunately, those four structures were not able to be measured, thus they are omitted in the results. Furthermore, the fifth waveguide was also discarded due to the high losses it presented.

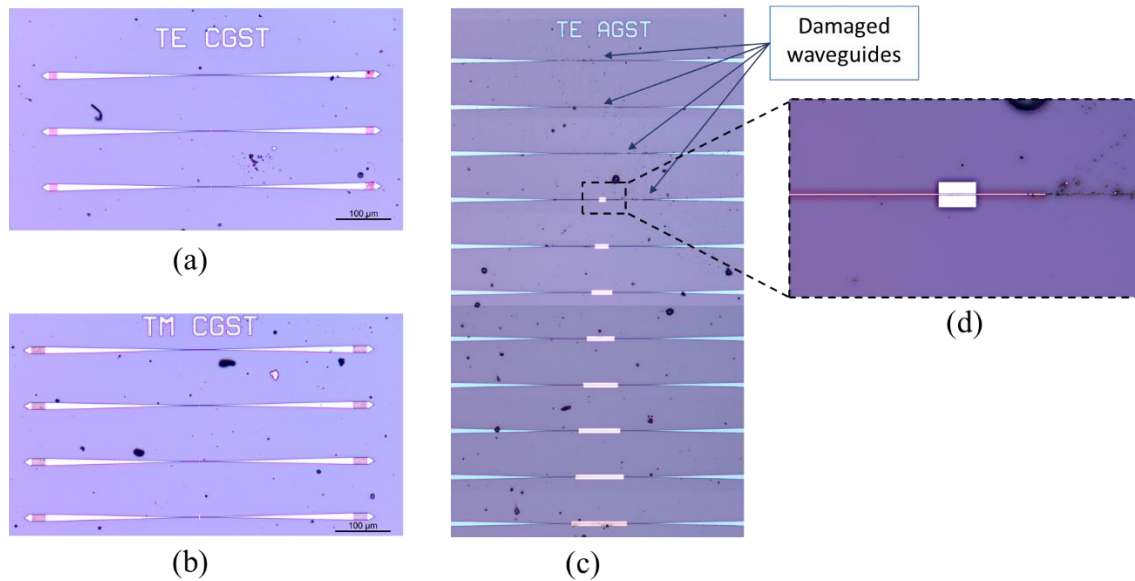


Fig. 30. Optical microscope images of waveguides for absorption characterisation. (a) x50 view of the first 3 TE waveguides for cGST characterisation. (b) x50 view of first 4 TM waveguides for cGST characterisation. (c) x10 view of the of the waveguides for aGST characterisation in TE polarization. (d) Zoom of a damaged (right) structure.

IV.3.2 Comparison of absorption between amorphous and crystalline

Since the GST is in amorphous state when fabricated, first measurements were done with the entire sample with aGST, corresponding to the results shown in Fig. 31(a), Fig. 33(a) and Fig. 34(a). Then, the sample was heated for 10 min at 250°C in N₂ using a rapid thermal annealing (RTA) furnace to change the GST from amorphous to crystalline. After this process, all the waveguides were measured again, obtaining the results shown in Fig. 31(b), Fig. 33(b) and Fig. 34(b).

Starting from TE polarization, the propagation losses in amorphous and crystalline are estimated. For aGST, due to the damage suffered by the waveguides designed for analysing its propagation losses, the measurements of the remaining waveguides were combined with the results of the “TE CGST” waveguides in amorphous state (Fig. 31(a)). Notice that these GST strips are short, but using both groups of waveguides, a good propagation loss estimation was achieved, as it will be shown below. On the other hand, for the estimation in crystalline state, the measurements of the “TE CGST” structures reported the results shown in Fig. 31(b). The spectral sweeps were done using a step of 1 nm.

On the left, in amorphous, the difference between waveguides is negligible due to the low absorption of the GST in such short patches. Meanwhile, when the sample is in crystalline state, it is possible to observe difference between waveguides. The longer the strips, the higher the attenuation, as predicted.

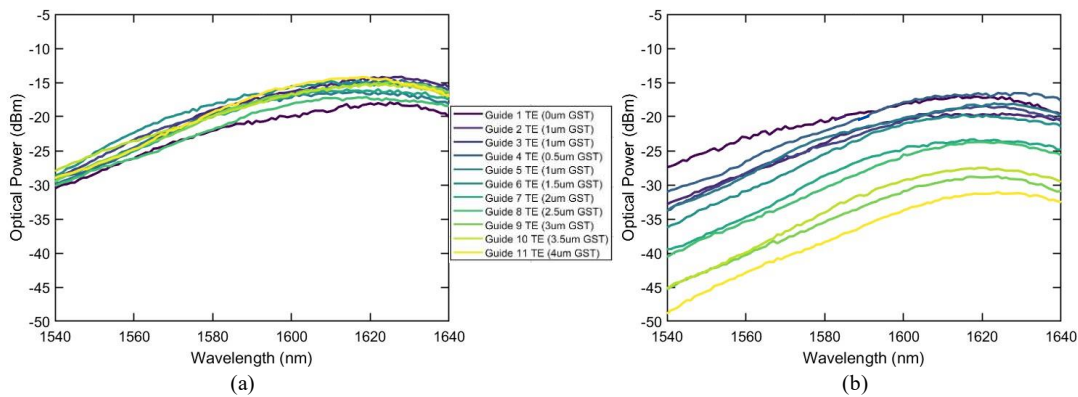


Fig. 31. Waveguides labelled as “TE CGST”. (a) Amorphous. (b) Crystalline.

Using the data presented Fig. 31, the propagation loss at 1550 nm for TE polarization was estimated by using linear regression, as shown in Fig. 32. Firstly, in Fig. 32(a) the values of the aGST measurements at 1550 nm with their corresponding regression line are represented. Analogously, the computation for crystalline state is shown in Fig. 32(b). Both results are in line with the predicted by simulations.

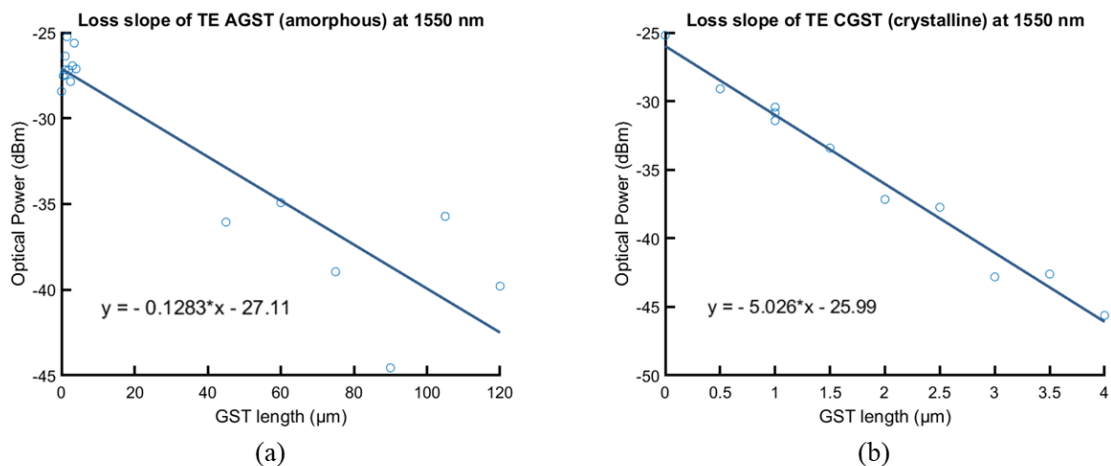


Fig. 32. Loss slope of GST in TE. (a) Amorphous state. (b) Crystalline state.

The second group of structures to analyse are the ones designed for characterisation in TM polarization, labelled in the chip as “TM AGST” and “TM CGST”. In this case, any waveguide was damaged, thus all of them were measured and their results are presented in Fig. 33 and Fig. 34. The results of the “TM AGST” structures are represented in Fig. 33. Here the differences in

aGST can be noticed on Fig. 33(a), where the variation between GST strips (20 μm) is enough to observe the change of the material in amorphous state. What is more, when GST turns crystalline (Fig. 33(b)), the absorption is so great that only the first five guides, whose lengths are 1 micron, can be measured.

On the other hand, the measurements for cGST characterisation are shown in Fig. 34. On the left, with the sample in amorphous state (Fig. 34(a)), most of the spectral sweeps are overlapped because of the low absorption of the GST in such short strips. Whereas, in crystalline state it is possible to observe the attenuation produced in the short GST patches, as depicted in Fig. 34(b).

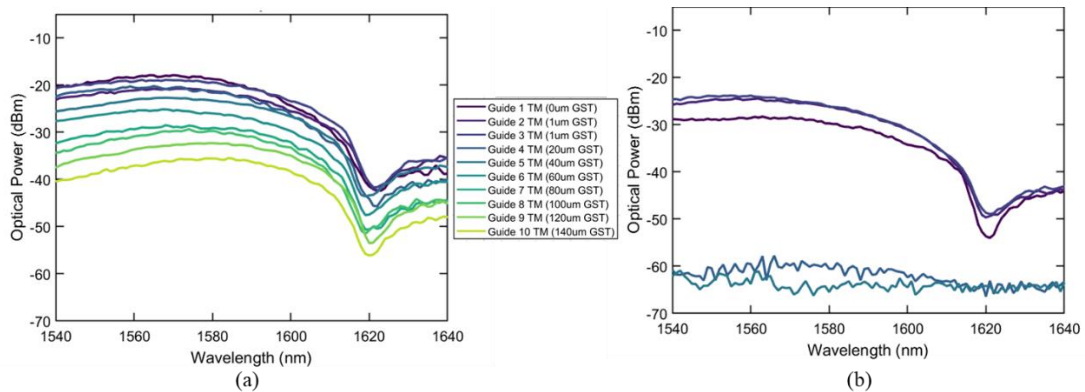


Fig. 33. Waveguides labelled as “TM AGST”. (a) Amorphous. (b) Crystalline.

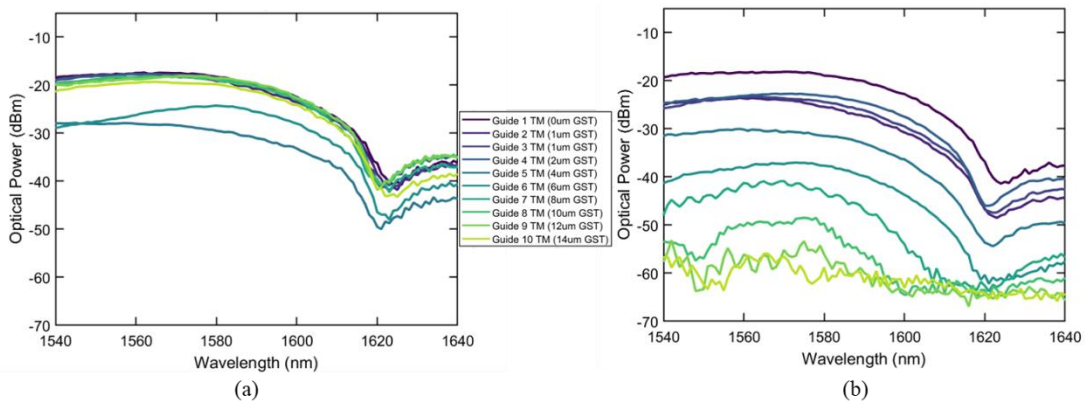


Fig. 34. Waveguides labelled as “TM CGST”. (a) Amorphous. (b) Crystalline.

Next two graphs in Fig. 35 show the loss slope of the GST in amorphous and crystalline states, which report a very accurate regression line. The reason behind is that the losses induced by the GST are much smaller than the deviation from the alignment and the grating couplers.

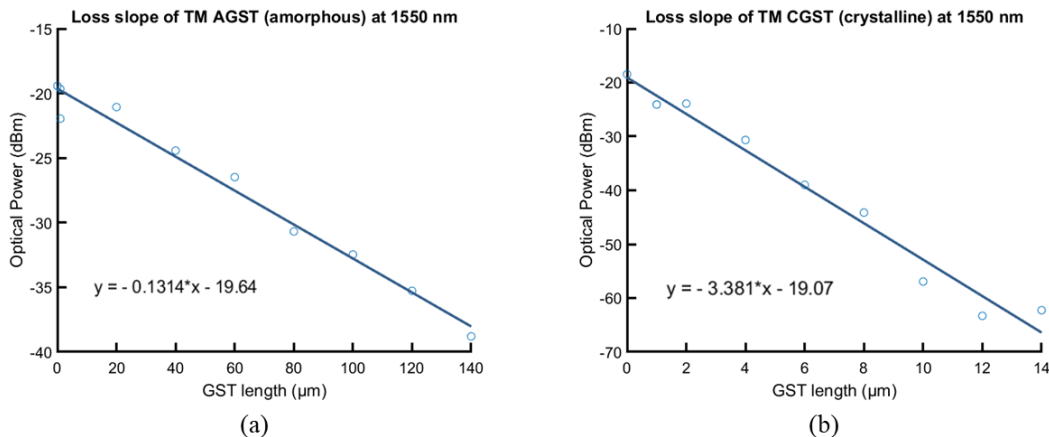


Fig. 35. Loss slope of GST in TM. (a) Amorphous state. (b) Crystalline state.

Table 7 lists both the simulated and experimental results of the propagation losses for the GST in amorphous and crystalline. Starting with TE polarization, the propagation loss estimation in amorphous is very similar between simulation and measurements (it presents a deviation lower than 0.1 dB/ μm). In crystalline, a large absorption change is noticed, in fair agreement with simulations. The discrepancies between simulation and measurements are attributed to deviations on the value of the refractive index considered for simulations. It should be noticed that rather large variations of the GST refractive indices have been reported depending on the used fabrication process [33].

TM polarization presents a similar behaviour. In amorphous, the predicted absorption is lower but on the same order of magnitude (it differs less than 0.3 dB/ μm). In crystalline state the difference between simulation and experimental results is about 2.6 dB/ μm , which is also reasonable due to variations in the GST refractive index.

Polarization	Sim. / Exp.	$\alpha_A(\text{dB}/\mu\text{m})$	$\alpha_C(\text{dB}/\mu\text{m})$
TE	Simulated	0.211	9.506
	Experimental	0.128	5.026
TM	Simulated	0.422	5.985
	Experimental	0.131	3.381

Table 7. Comparison of propagation losses of hybrid GST/Si waveguide in TE and TM.

IV.3.3 All-optical switching

The setup designed for demonstrating all-optical switching has been presented in Fig. 28. By using the devices described there, it is possible to generate an optical pulse of 200-ns-wide which leads the transition to amorphous from crystalline. To demonstrate that behaviour, any GST strip could be chosen. For each pulse, a small portion of GST was heated up above the melting point (650°C) followed by a fast cooling ($> 1^\circ\text{C}/\text{ns}$). Such high cooling rates are required to melt-quench the GST and avoid recrystallization. Considering this, the GST strip used was 3.5- μm -long.

Peak power is the other variable involved in the transition. It is important to deliver enough power to induce the change, but not so high that it damages the structure. In order to guarantee the correct value, testing with another waveguide was done. If the power is lower than the one needed for the transition, the material remains in crystalline state without affecting its properties. However, if the peak power is too high, the GST ablates and it is removed from the waveguide, thus reducing the optical losses. In Fig. 36 there is an example of an image taken with the microscope after injecting a very strong optical pulse.

To induce the change to amorphous, the output power of the EDFA is 35 mW. Therefore, the power reaching the sample is ~ 7 nJ. After the losses in the set-up and the attenuation because of the gratings, the energy in the chip for switching from crystalline to amorphous is about a few hundred pJ. On the other hand, if the output power is more than 100 mW, it is possible to damage the structure, like the example shown in Fig. 36. On the image, the left side of the GST strip is burned. However, the silicon waveguide under the damaged GST layer is still working. Therefore, the measurements of that structure reported lower losses due to the ablation produced in the GST.

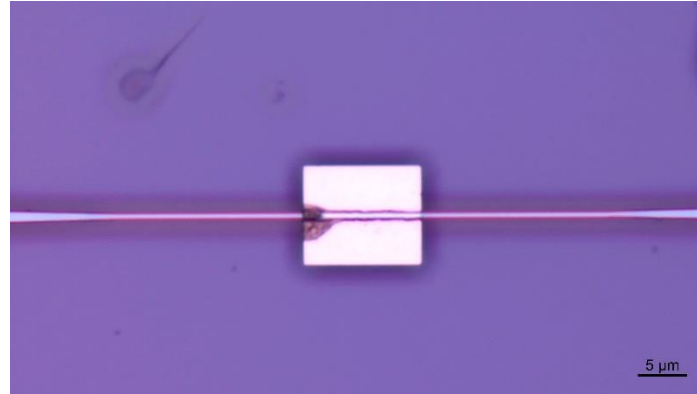


Fig. 36. Microscope image of a GST strip ablated after a strong optical pulse.

As it was previously mentioned, going back to cGST is not that simple. The sample needs to be heated in a uniform way, apart from controlling the optical power to avoid damage. Due to this, if a small pulse is injected, the change in the material is produced only in a couple of microns. To avoid this problem, one possibility is injecting a wider optical pulse (e.g., 1 μ s), but the low absorption of the GST produces that the material does not change uniformly. Another option reported could be using a pulse train with different amplitudes and widths, but the implementation of this technique is not so easy and, therefore, it was not considered in this work. Finally, the method employed to recover the GST in crystalline state was injecting a continuous power of 55 mW at the output of the EDFA. The reason behind this technique is that one part of GST turns crystalline and then, due to the higher absorption of that portion, a gradual change takes place, as depicted on the right side of Fig. 37. In the left side of the picture there is a graph with four cycles of switching, where it is clearly shown that the propagations losses changed significantly. However, taking into account the estimations proposed in Table 7, the attenuation should be higher. The lower value is due to the mixed stated mentioned before, as it is shown in Fig. 38. On the left in Fig. 38(a) there is a waveguide with a 3- μ m-long GST strip in crystalline state, which can be appreciated with the blue colour it presents. On the other hand, Fig. 38(b) shows a 3.5- μ m-long patch where the GST is in a mixed state (amorphous at the beginning and then, crystalline). Notice that after any alteration, GST maintains its state indefinitely until a new optical pulse is injected (non-volatile switching performance).

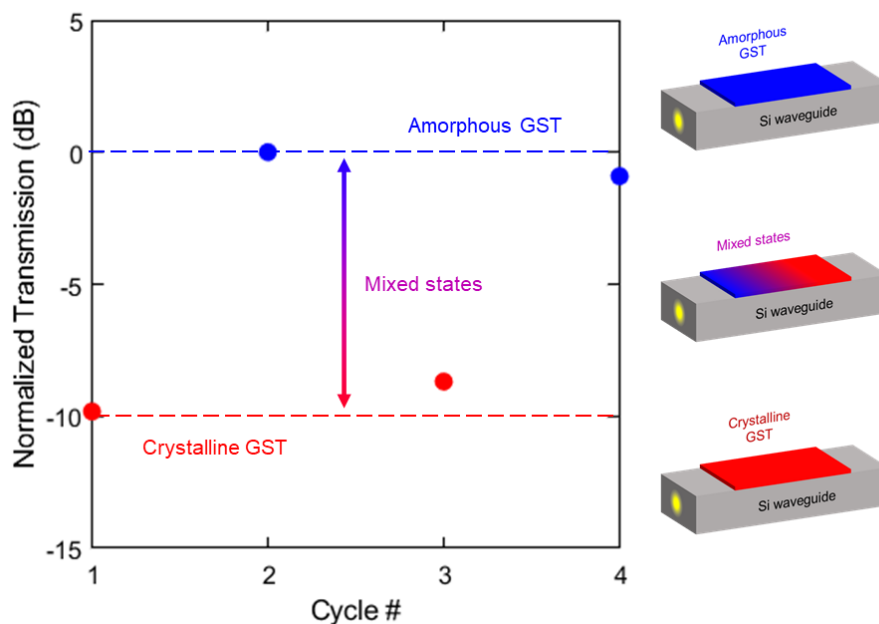


Fig. 37. Four cycles of all-optical switching in a 3.5- μ m-long waveguide at 1550 nm and TE polarization.

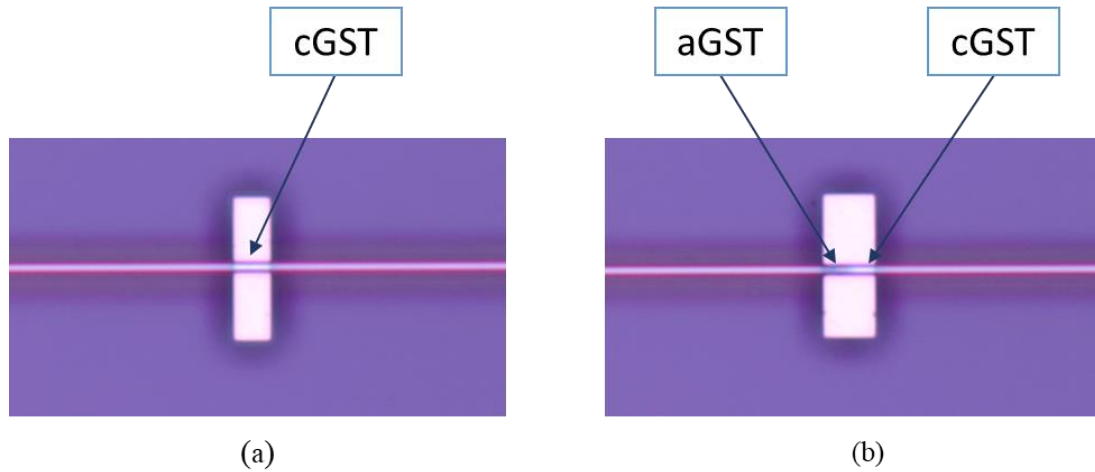


Fig. 38. Straight waveguides with GST strips in amorphous and crystalline. (a) 3 μm in crystalline state (cGST). (b) 3.5 μm in mixed states (aGST and cGST).

IV.4 Characterisation of phase switching

IV.4.1 Images of ring resonators for phase shift characterisation

The fabricated structures for phase shift variation analysis are presented in Fig. 39. Both images at the top correspond with a x10 view of the first TE/TM rings, while the images on the bottom correspond with a x100 view of the first ring of each group of structures. On them it is possible to appreciate the 500-nm-long GST patches deposited on the rings.

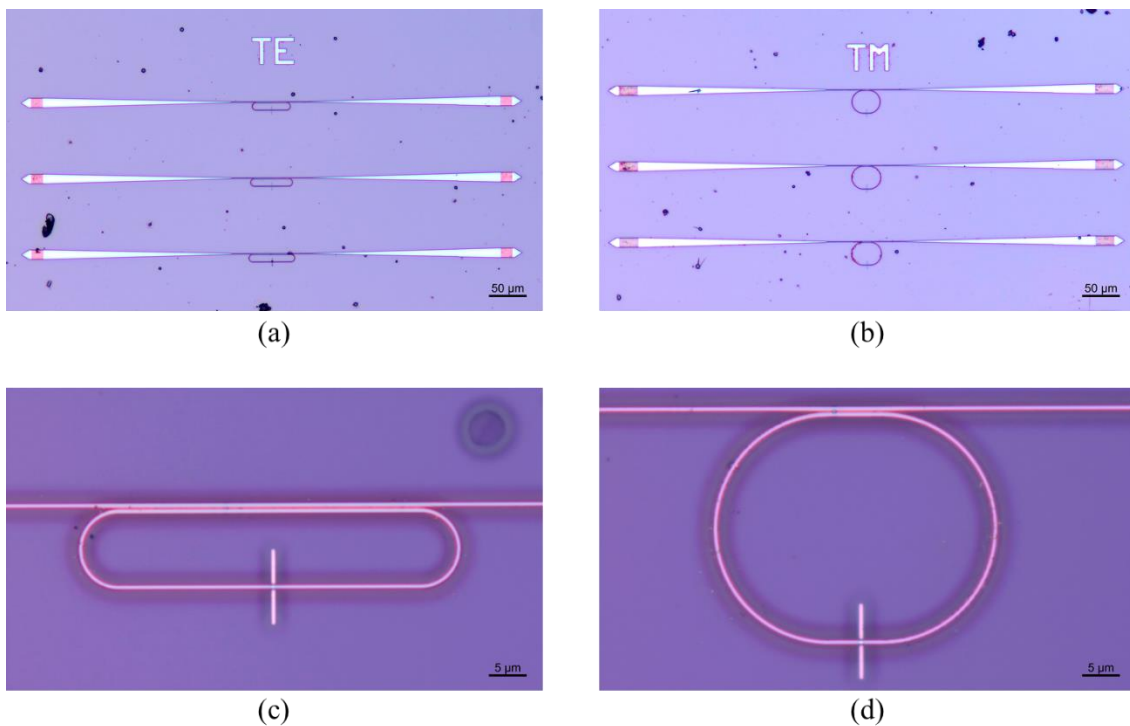


Fig. 39. Microscope images of the fabricated ring resonators. (a) First three TE rings. (b) First three TM rings. (c) TE ring 1 ($L_c = 40 \mu\text{m}$) with a 500-nm-long GST strip. (d) TM ring 1 ($L_c = 7 \mu\text{m}$) with a 500-nm-long GST strip.

IV.4.2 Analysis of phase shift variation between amorphous and crystalline

As the sample is in amorphous state when fabricated, the measurements depicted in Fig. 40 correspond to the performance of the rings for aGST. They represent a spectral sweep of the TE rings using a step of 0.1 nm, where it is possible to find the optimal structures (i.e., with maximum extinction ratio).

Again, the influence of the response of the grating couplers can be clearly observed. Normalizing the measurements by using the envelope of the signals would be possible. However, it is also interesting to maintain the information about losses for demonstrating the all-optical switching performance.

High extinction ratios are desired, thus the rings named as 1, 3, 4, 5, 8 and 9 are the most interesting ones from this point of view. Another choosing criteria is that the optimal performance of the EDFA is achieved at ~ 1560 nm, thus the higher values around this wavelength are preferred. Considering these reasons, the best structures in TE polarization could be rings 1, 3, 4 and 5.

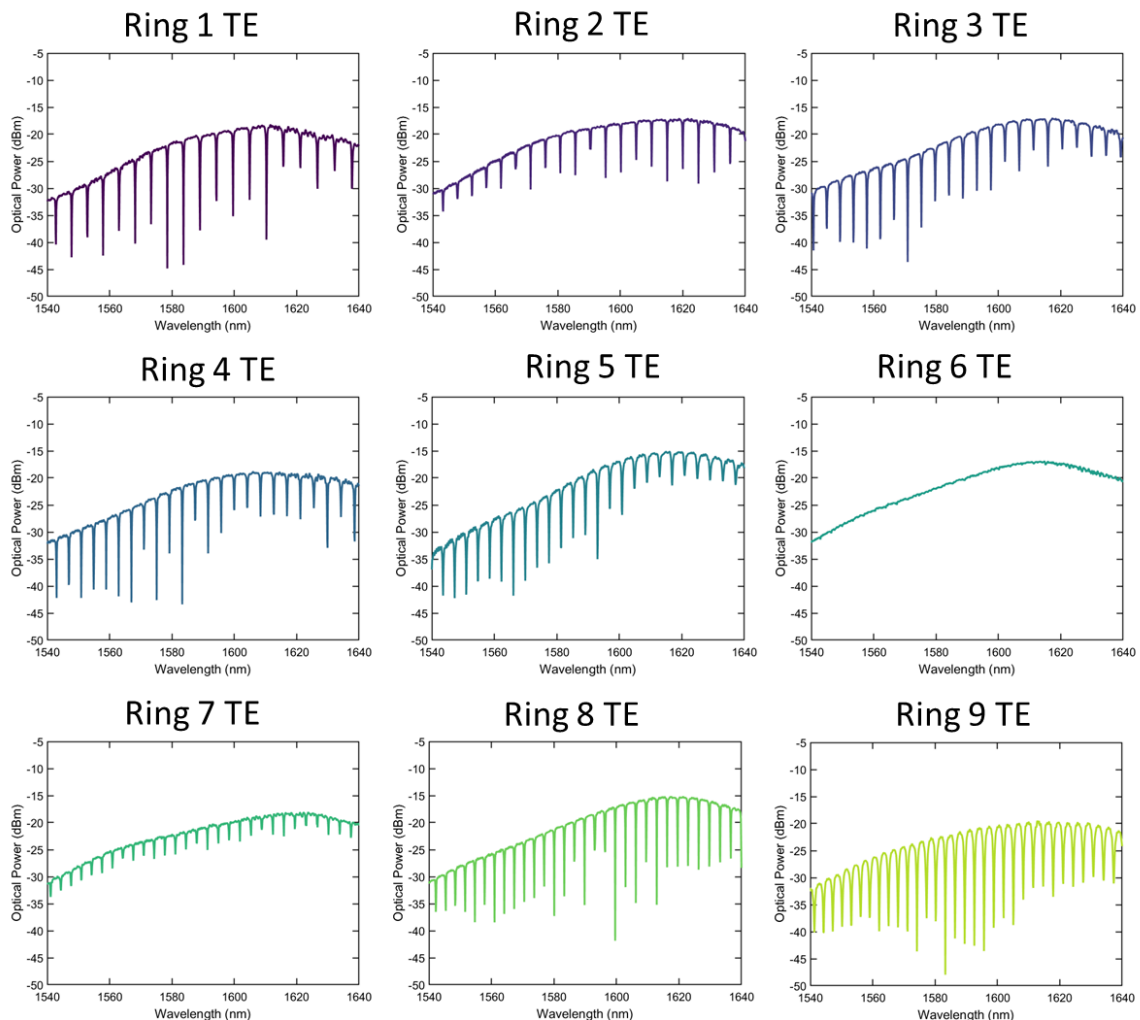


Fig. 40. Spectrum of ring resonators from 1 to 9 in TE polarization.

Analogously, Fig. 41 shows the response of the measured rings for TM polarization. The criteria to select the best performances is the same mentioned above, thus rings 3, 4, 5 and 6 would be the preferred ones.

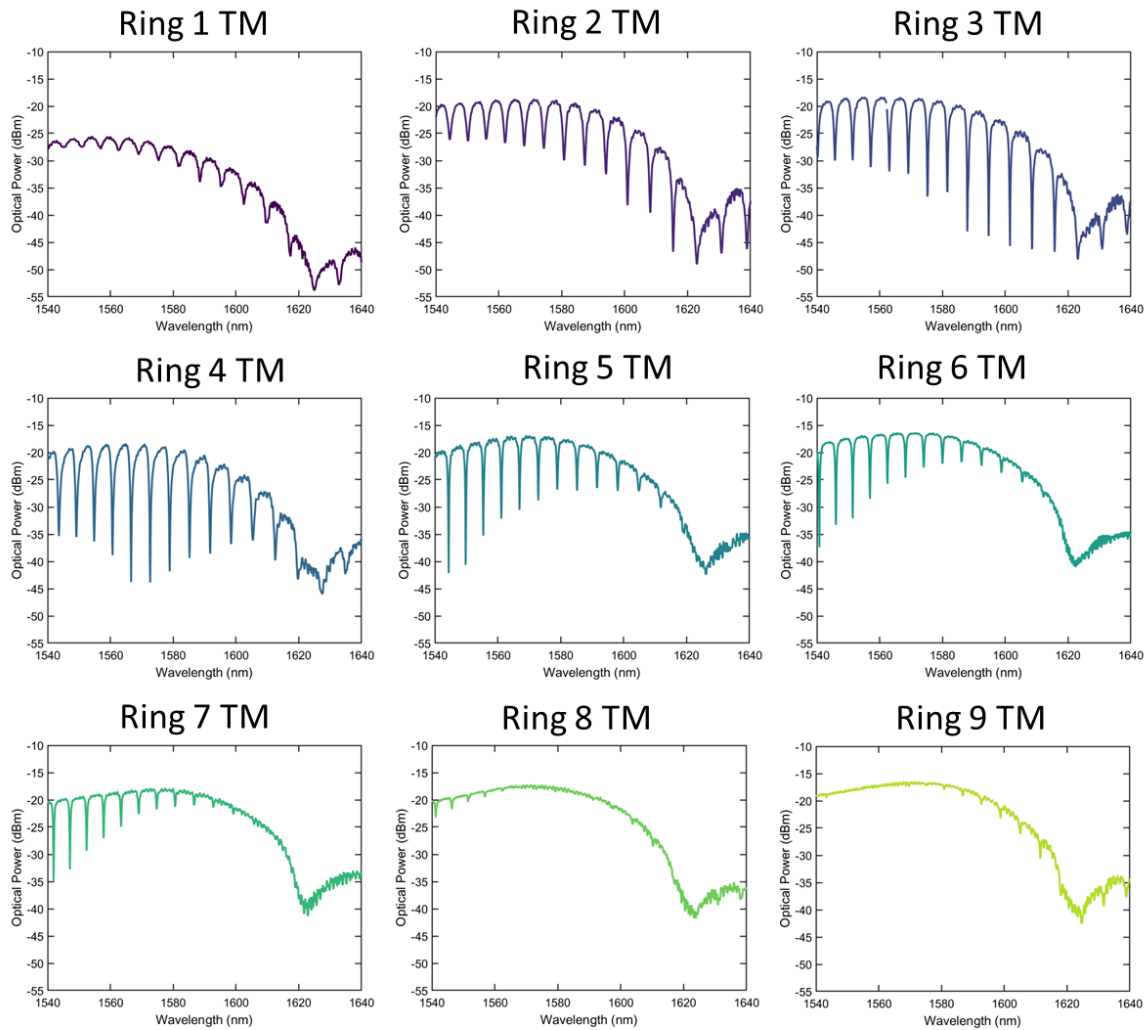


Fig. 41. Spectrum of ring resonators from 1 to 9 in TM polarization.

After finding the optimum rings in amorphous state, the comparison of their results with the measurements of the sample in crystalline state is done. At this point the strategy is analysing the performance in a shorter spectrum range (e.g., 10 nm) with higher resolution (0.01 nm). They are around the center frequency of the third optical window (C-band), which is used for telecom applications. The measurements presented below have been made by selecting a range of 10 nm on that wavelength range, containing at least two resonances. Here, the information about the attenuation is not relevant. Therefore, the measurements have been normalised by using the maximum of the response in the region of interest.

Starting with TE polarization, the two selected responses are shown in Fig. 42. On the one hand, in Fig. 42(a) the measurements of Ring 3 for TE polarization are represented, where it is possible to see a phase shift variation ($\Delta\lambda_{RES}$) of 0.7 nm. This value corresponds with the design condition (phase shift variation of $\pi/4$). However, the attenuation has not changed as expected. According to the simulations shown in previous sections, the extinction ratio should vary when the phase change is produced. Therefore, if the resonance has moved but the extinction ratio maintains its value, it is possible that the coupling length selected coincides with a value where both coupling

coefficients for aGST and cGST are similar. Meanwhile ring 5 (Fig. 42(b)) shows minor changes between the responses of amorphous and crystalline states, since the resonances in aGST and cGST are overlapped. Therefore, it cannot be used to demonstrate the switching performance.

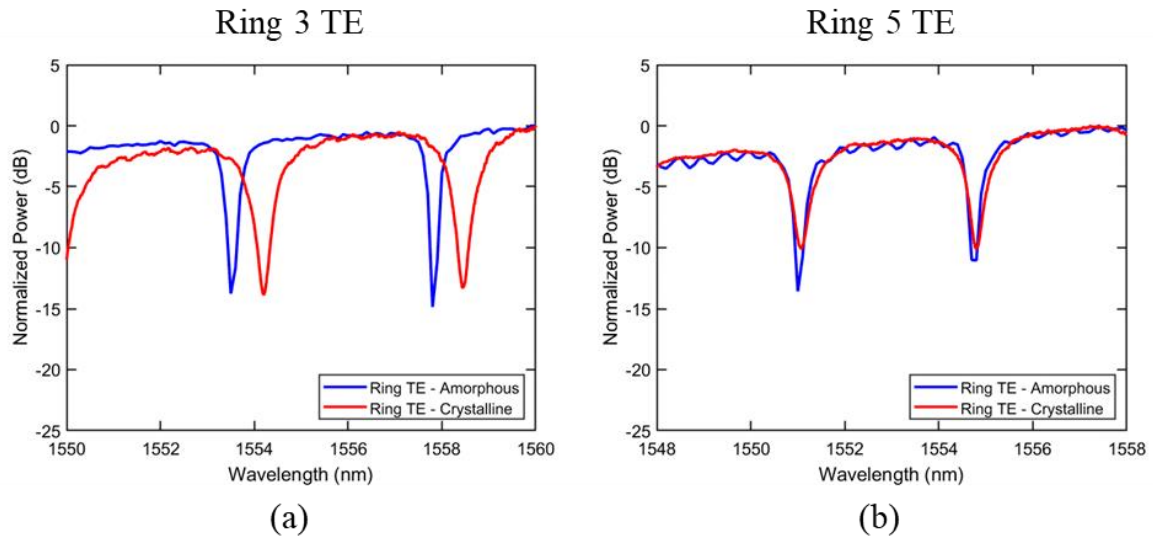


Fig. 42. Comparison of the spectral responses in aGST and cGST of two rings in TE polarization. (a) TE ring 3. (b) TE ring 5.

Similarities with the results presented before are shown for TM polarization in Fig. 43. Ring 4 does not change his performance when changing between amorphous and crystalline. Meanwhile, rings 6 vary the extinction ratio and the resonance wavelength, which was the expected behaviour.

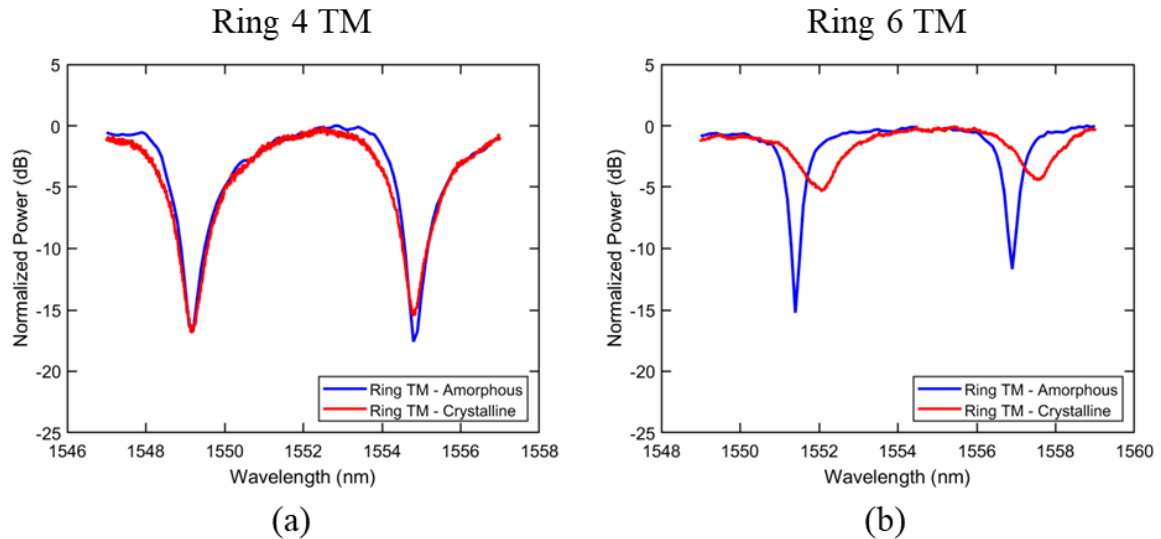


Fig. 43. Comparison of the spectral responses in aGST and cGST of two rings in TM polarization. (a) TM ring 4. (b) TM ring 6.

All things considered, there are various rings that could be used to demonstrate the phase shift variation. Due to the measured results, the chosen ring for all-optical switching is the fifth, as it will be shown in next section. It presents not only a large variation in the resonant wavelength but also a change in the extinction ratio above 10 dB. This makes sense because the propagation loss is over one order of magnitude higher when GST is in crystalline state.

By using the equation (7) and the values presented in Table 3, the phase shift per unit length was calculated. The comparison between simulated and experimental results is presented in Table 8,

where it is possible to observe that despite minor discrepancies, these measurements are in good agreement with simulations.

$$\Delta\beta = 2\pi \frac{\Delta\lambda}{FSR} \cdot \frac{1}{L_{GST}} \quad (7)$$

Polarization	Sim. / Exp.	$\Delta\beta$ (rad/ μm)
TE	Simulated	0.4265π
	Experimental	0.6588π
TM	Simulated	0.5570π
	Experimental	0.5090π

Table 8. Comparison of phase shift of hybrid GST/Si rings in TE and TM.

IV.4.3 All-optical switching

Taking into account the results presented in the previous section, all-optical switching will be performed on the fifth ring resonator for TM polarization. It is the structure that presents the best behaviour both in terms of insertion loss and extinction ratio.

After the rapid thermal annealing that was previously mentioned, the GST on the chip is in crystalline, thus the switching will lead the transition from cGST to aGST by using the setup presented in Fig. 28. At this point, there is an important difference between the switching technique employed in waveguides and the method used for rings. In order to induce the phase change on ring resonators, focusing the optical power in one resonance is required. Therefore, if more than one pulse is needed, it would be necessary to tune the wavelength in the resonance as many times as optical pulses are injected. In the example shown below the resonance selected is around 1562 nm because it is the range where the EDFA employed performs the best in terms of stability.

The comparison between the simulations and the measurements of all-optical switching in rings is shown in Fig. 44. By applying various optical pulses (and focusing the resonance, which has moved with each pulse), the result obtained is shown in Fig. 44(b). Starting from the cGST state (red line), the resonance has moved 0.55 nm to the left when applying various optical pulses. Moreover, the extinction ratio changed 11 dB, demonstrating the all-optical switching desired, which is in good agreement with the simulation shown in Fig. 44(a).

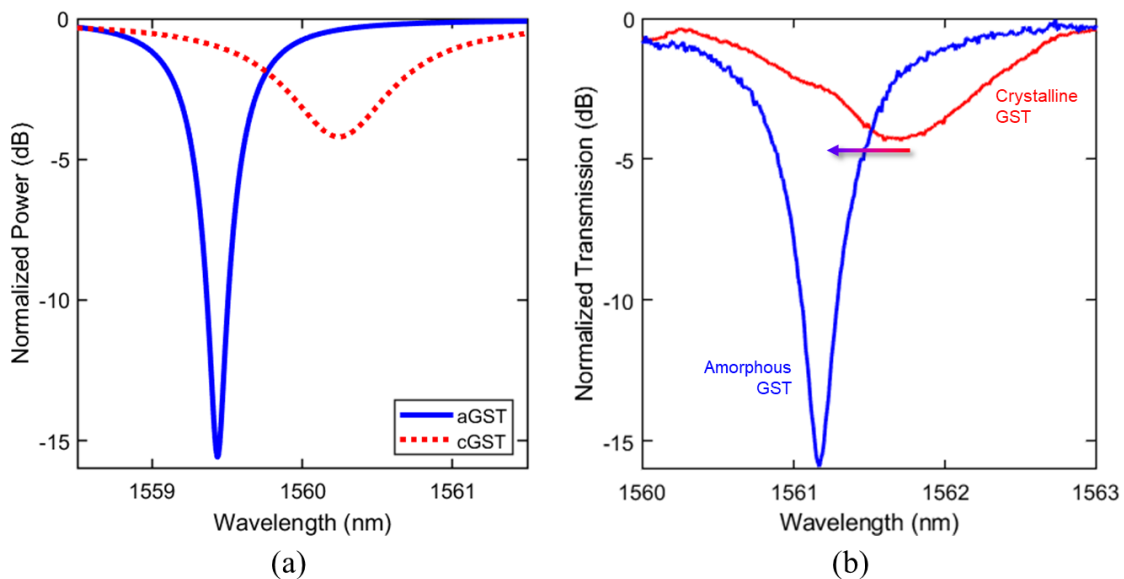


Fig. 44. One resonance of the TM ring 5 after performing all-optical switching. (a) Simulation results. (b) Experimental results.

V. Conclusions and future work

V.1 Conclusions

The growth of data consumption in the last decade have powered the development of new photonics systems. From the point of view of users, smaller devices are required, whereas from the side of the network, data centers handle more and more information every day.

Integrated photonics is presented as a solution, offering faster speed and higher bandwidth than electronic systems, as well as a lower power consumption. Moreover, the combination with phase change materials could convert this platform in a cutting-edge technology due to the miniaturisation capabilities and the energy saving. Vanadium dioxide or germanium-antimony-tellurides are considered as promising materials to develop hybrid CMOS-compatible systems. In particular, GST stands out due to the large and non-volatile variation of its refractive index when switching between an amorphous and crystalline state.

Throughout this research, the optical performance of hybrid Si/GST waveguides has been analysed, taking advantage of the non-volatile property of GST. An integrated photonic chip was designed and experimentally characterized. The transition between amorphous and crystalline has been measured, analysing the propagation losses by using hybrid Si/GST waveguides and determining the phase shift variation utilizing ring resonator structures. Simulations with RSoft software have been done to perform this work, apart from the measurements in the laboratory and the data processing with MATLAB.

By using an optimal thickness for the GST layer in order to avoid the formation of higher-order modes, high-performance all-optical switching in different type of Si/GST hybrid structures has been demonstrated. Both large extinction ratios and phase shifts of around $5 \text{ dB}/\mu\text{m}$ and $\pi/2 \text{ rad}/\mu\text{m}$, respectively, have been measured. By employing a ring resonator, an extinction ratio above 10 dB and almost negligible insertion losses have been achieved when the GST switched between amorphous and crystalline states. These results can be used to create new Si/GST devices for integrated photonic applications, such as optical switches, optical memories, ultra-low power photonic integrated circuits, artificial photonic neuronal networks, among others. Therefore, phase change materials and particularly GST are establishing themselves as one of the technologies that could play a key role in the short and long-term photonics devices.

V.2 Future work

Despite the positive results reported, the temporal dynamics of the hybrid structures has not been measured yet. To this end, the setup used for all-optical switching needs to be adjusted in order to perform such measurements in the time domain. This characterisation would be interesting for enabling our devices for practical switching or modulation applications.

On the other hand, inducing the transition from amorphous to crystalline should be analysed because it is not as simple as the reverse. A technique to heat the active material in a uniformly way, such as the using of a pulse train with different widths and amplitudes, could be interesting to investigate. Furthermore, the switching techniques in rings are also problematic due to the requirement of finding the resonance and inject the pulse exactly on that point. A more detailed analysis is required to optimize the switching performance.

Finally, GST is a material that can get oxidized if not protected with an upper-cladding, such as SiO₂ [40] or ITO [19]. In this study, the SiO₂ cladding has not been deposited, thus the GST can deteriorate if a large number of switching cycles is performed. Therefore, it would be desirable to evaluate such issue with and without the SiO₂ cladding.

References

- [1] G. Lifante, "Introduction to Integrated Photonics," *Integr. Photonics Fundam.*, pp. 1–23, 2005, doi: 10.1002/0470861401.ch1.
- [2] L. A. Coldren, *Diode Lasers and Photonic Integrated Circuits.*, 2nd ed. Hoboken: John Wiley & Sons, Incorporated, 2012.
- [3] L. Thylén and L. Wosinski, "Integrated photonics in the 21st century," *Photon. Res.*, vol. 2, no. 2, pp. 75–81, 2014, doi: 10.1364/PRJ.2.000075.
- [4] T. Aalto, M. Cherchi, M. Harjanne, F. Sun, and M. Kapulainen, *3Mm Silicon Photonics*. 2018.
- [5] A. Rickman, "The commercialization of silicon photonics," *Nat. Photonics*, vol. 8, no. 8, pp. 579–582, 2014, doi: 10.1038/nphoton.2014.175.
- [6] R. Soref and J. Lorenzo, "All-silicon active and passive guided-wave components for $\lambda = 1.3$ and $1.6 \mu\text{m}$," *IEEE J. Quantum Electron.*, vol. 22, no. 6, pp. 873–879, 1986, doi: 10.1109/JQE.1986.1073057.
- [7] J. Chiles and S. Fathpour, "Silicon photonics beyond silicon-on-insulator," 2017.
- [8] A. J. Shaikh and O. Sidek, "Making Silicon Emit Light Using Third Harmonic Generation," *Procedia Eng.*, vol. 29, pp. 1456–1461, 2012, doi: <https://doi.org/10.1016/j.proeng.2012.01.154>.
- [9] K. J. Miller, R. F. Haglund, and S. M. Weiss, "Optical phase change materials in integrated silicon photonic devices: review," *Opt. Mater. Express*, vol. 8, no. 8, p. 2415, 2018, doi: 10.1364/ome.8.002415.
- [10] S. Cueff *et al.*, "VO2 nanophotonics," *APL Photonics*, vol. 5, no. 11, 2020, doi: 10.1063/5.0028093.
- [11] Q. Zhang, Y. Zhang, J. Li, R. Soref, T. Gu, and J. Hu, "Broadband nonvolatile photonic switching based on optical phase change materials: beyond the classical figure-of-merit," *Opt. Lett.*, vol. 43, no. 1, p. 94, 2018, doi: 10.1364/ol.43.000094.
- [12] K. Shibuya *et al.*, "Switching dynamics of silicon waveguide optical modulator driven by photothermally induced metal-insulator transition of vanadium dioxide cladding layer," *Opt. Express*, vol. 28, no. 25, p. 37188, 2020, doi: 10.1364/oe.409238.
- [13] H. M. K. Wong *et al.*, "Broadband, Integrated, Micron-Scale, All-Optical Si₃N₄/VO₂ Modulators with pJ Switching Energy," *ACS Photonics*, vol. 6, no. 11, pp. 2734–2740, 2019, doi: 10.1021/acsp Photonics.9b00708.
- [14] M. R. Otto *et al.*, "How optical excitation controls the structure and properties of vanadium dioxide," *Proc. Natl. Acad. Sci. U. S. A.*, vol. 116, no. 2, pp. 450–455, 2019, doi: 10.1073/pnas.1808414115.
- [15] A. Joushaghani, J. Jeong, S. Paradis, D. Alain, J. Stewart Aitchison, and J. K. S. Poon, "Wavelength-size hybrid Si-VO₂ waveguide electroabsorption optical switches and photodetectors," *Opt. Express*, vol. 23, no. 3, p. 3657, 2015, doi: 10.1364/oe.23.003657.
- [16] E. Kuramochi and M. Notomi, "Optical memory: Phase-change memory," *Nat. Photonics*, vol. 9, no. 11, pp. 712–714, 2015, doi: 10.1038/nphoton.2015.212.
- [17] W. H. P. Pernice and H. Bhaskaran, "Photonic non-volatile memories using phase change materials," *Appl. Phys. Lett.*, vol. 101, no. 17, 2012, doi: 10.1063/1.4758996.
- [18] C. Rios, P. Hosseini, C. D. Wright, H. Bhaskaran, and W. H. P. Pernice, "On-chip photonic memory elements employing phase-change materials," *Adv. Mater.*, vol. 26, no. 9, pp. 1372–1377, 2014.
- [19] J. Zheng *et al.*, "GST-on-silicon hybrid nanophotonic integrated circuits: a non-volatile quasi-continuously reprogrammable platform," *Opt. Mater. Express*, vol. 8, no. 6, p. 1551, 2018, doi: 10.1364/ome.8.001551.
- [20] H. A. Z. Hang, X. I. N. G. Y. Ang, L. I. Lu, J. I. C. Hen, R. Ahman, and L. I. Z. Hou, "Comparison of phase change process in Si-GST hybrid integrated waveguide and MMI devices," vol. 5.

- [21] H. H. U. Ao *et al.*, “Contra-directional switching enabled by Si-GST grating,” vol. 28, no. 2, pp. 1574–1584, 2020.
- [22] G. Sb, Z. Yu, J. Zheng, P. Xu, W. Zhang, and Y. Wu, “Ultracompact Electro-Optical Modulator-Based Ge₂Sb₂Te₅ on Silicon,” vol. 30, no. 3, pp. 250–253, 2018.
- [23] Z. Cheng, C. Ríos, W. H. P. Pernice, C. D. Wright, and H. Bhaskaran, “On-chip photonic synapse,” *Sci. Adv.*, vol. 3, no. 9, p. e1700160, Sep. 2017, doi: 10.1126/sciadv.1700160.
- [24] I. Chakraborty, G. Saha, A. Sengupta, and K. Roy, “Toward Fast Neural Computing using All-Photonic Phase Change Spiking Neurons,” *Sci. Rep.*, no. August, pp. 1–9, 2018, doi: 10.1038/s41598-018-31365-x.
- [25] S. K. Patel, J. Parmar, V. Sorathiya, and T. K. Nguyen, “Tunable infrared metamaterial - based biosensor for detection of hemoglobin and urine using phase change material,” *Sci. Rep.*, pp. 1–11, 2021, doi: 10.1038/s41598-021-86700-6.
- [26] H. Urgelles, “Demostración de dispositivos fotónicos basados en Silicio/GST con respuesta no-volátil,” Universidad Politécnica de Valencia, 2020.
- [27] H. Zhang *et al.*, “Miniature Multilevel Optical Memristive Switch Using Phase Change Material,” *ACS Photonics*, vol. 6, no. 9, pp. 2205–2212, 2019, doi: 10.1021/acsp Photonics.9b00819.
- [28] K. Kato, M. Kuwahara, H. Kawashima, T. Tsuruoka, and H. Tsuda, “Current-driven phase-change optical gate switch using indium-tin-oxide heater,” *Appl. Phys. Express*, vol. 10, no. 7, pp. 3–6, 2017, doi: 10.7567/APEX.10.072201.
- [29] H. Zhang *et al.*, “Nonvolatile waveguide transmission tuning with electrically-driven ultra-small GST phase-change material,” *Sci. Bull.*, vol. 64, no. 11, pp. 782–789, 2019, doi: 10.1016/j.scib.2019.04.035.
- [30] J. Zheng *et al.*, “Nonvolatile Electrically Reconfigurable Integrated Photonic Switch Enabled by a Silicon PIN Diode Heater,” *Adv. Mater.*, vol. 32, no. 31, pp. 1–8, 2020, doi: 10.1002/adma.202001218.
- [31] Y. Wang *et al.*, “Electrical tuning of phase-change antennas and metasurfaces,” *Nat. Nanotechnol.*, vol. 16, no. 6, pp. 667–672, 2021, doi: 10.1038/s41565-021-00882-8.
- [32] I. Olivares *et al.*, “Optical switching in hybrid VO₂/Si waveguides thermally triggered by lateral microheaters,” *Opt. Express*, vol. 26, no. 10, p. 12387, 2018, doi: 10.1364/oe.26.012387.
- [33] M. S. Nisar, X. Yang, L. Lu, J. Chen, and L. Zhou, “On-Chip Integrated Photonic Devices Based on Phase Change Materials,” 2021.
- [34] Y. Ikuma *et al.*, “Small-sized optical gate switch using Ge₂Sb₂Te₅ phase-change material integrated with silicon waveguide,” *Electron. Lett.*, vol. 46, no. 5, pp. 368–369, 2010, doi: 10.1049/el.2010.3588.
- [35] D. Tanaka *et al.*, “Ultra-small, selft-holding, optical gate switch using Ge₂Sb₂Te₅ with a multi-mode Si waveguide,” *Opt. Express*, vol. 20, no. 9, pp. 442–445, 2012.
- [36] M. Rudé *et al.*, “Optical switching at 1.55 μm in silicon racetrack resonators using phase change materials,” *Appl. Phys. Lett.*, vol. 103, no. 14, pp. 2–6, 2013, doi: 10.1063/1.4824714.
- [37] X. Li *et al.*, “Experimental investigation of silicon and silicon nitride platforms for phase-change photonic in-memory computing,” *Optica*, vol. 7, no. 3, p. 218, 2020, doi: 10.1364/optica.379228.
- [38] H. Zhang, L. Zhou, J. Xu, L. Lu, J. Chen, and B. M. A. Rahman, “All-optical non-volatile tuning of an AMZI-coupled ring resonator with GST phase-change material,” *Opt. Lett.*, vol. 43, no. 22, p. 5539, 2018, doi: 10.1364/ol.43.005539.
- [39] C. Rios *et al.*, “Integrated all-photonic non-volatile multi-level memory,” *Nat. Photonics*, vol. 9, no. 11, pp. 725–732, 2015, doi: 10.1038/nphoton.2015.182.
- [40] R. Golovchak *et al.*, “Oxygen incorporation into GST phase-change memory matrix,” *Appl. Surf. Sci.*, vol. 332, pp. 533–541, 2015, doi: <https://doi.org/10.1016/j.apsusc.2015.01.203>.

Appendix I. Poster for SPPM2021 international online conference

Poster presented in the SPPM2021 international online conference on June 10th.

Spintronics
Photonics
Phononics
Magneto-Optics

ONLINE INTERNATIONAL CONFERENCE

June 10, 2021

NANOPHOTONICS
TECHNOLOGY
CENTER

UNIVERSITAT
POLITÈCNICA
DE VALÈNCIA

High-performance optical switches based on GST/Si waveguides

Alejandro Santomé^{1,*}, Helen Urgelles¹, Jorge Parra¹ and Pablo Sanchis^{1,*}
¹Nanophotonics Technology Center, Universitat Politècnica de València, Camino de Vera s/n, 46022 Valencia, Spain
 E-mail: *alsanva3@teleco.upv.es, *pabsanki@ntc.upv.es

Web: www.ntc.upv.es

Abstract

We present a high-performance non-volatile optical switch by utilizing a 25-nm-thick Ge₂Sb₂Te₅ (GST) layer on Si waveguides and optical ring resonators. Optical switching at telecom wavelengths using subwavelength active lengths is possible due to the large variation in the GST refractive index between the crystalline and amorphous state. By leveraging such properties and optimizing the thickness of the GST layer, our experimental devices feature a high extinction ratio together with low insertion losses in ultra-compact footprints.

GST/Si waveguide properties

The GST thickness was optimized (25 nm) by simulation at $\lambda = 1550$ nm to avoid coupling of undesired high-order optical modes.

Propagation losses		Phase shift	
$\alpha = \frac{20 \log_{10}(e)}{\lambda} 2\pi \text{Im}(n_{\text{eff}})$	$\phi = \frac{2\pi}{\lambda} \text{Re}(n_{\text{eff}})$		
TE	0.221	9.507	
TM	0.422	5.986	
TE	10.82	8.195	
TM	11.972	9.591	

Amorphous GST
 $n_{\text{eff}} = 2.62 \pm 0.005$

Crystalline GST
 $n_{\text{eff}} = 2.95 \pm 0.027$

Experimental GST/Si devices

GST/Si waveguides and ring resonators were designed, fabricated and characterized. Initially, the GST is deposited in the amorphous state. Crystallization was achieved by heating the sample for 10 min at 250 °C in N₂ using a rapid thermal annealing (RTA) furnace.

On-chip all-optical switching

GST/Si waveguide

Transition between crystalline and amorphous state can be directly achieved by injecting a strong in-plane optical pulse. However, the length of the GST layer produces the appearance of intermediate states where the material is mixed between amorphous-crystalline. Thus, when an optical pulse is injected into the waveguide, only a short section of the GST changes its state immediately. The remaining material will make the transition after receiving a new optical pulse. In this situation, the crystalline layer absorbs most of the power, heating the material and enabling the change between states. After any alteration, GST maintains its mode indefinitely until a new optical pulse is injected (non-volatile).

GST/Si ring resonator

Changing states in a ring resonator is quite more complex because it is necessary to employ exactly the pulse power required to make the transition in the resonance wavelength.

Taking into account the refractive index of GST in both states, it is expected to find a wavelength shift to the right when changing to crystalline. Furthermore, the extinction ratio (ER) varies significantly because the propagation loss is over one order of magnitude higher when GST is in crystalline mode.

Conclusions

High-performance all-optical switching using GST/Si waveguides has been demonstrated. The optimal GST thickness has been analyzed and experimentally tested to avoid coupling of undesired high-order modes. Non-volatile optical switching with a high extinction ratio and negligible insertion losses have been demonstrated by using a ring resonator with an ultra-short 500-nm-long GST/Si waveguide. Furthermore, the possibility of achieving intermediate optical states has also been shown.

Acknowledgements & References

Financial support from Ministerio de Ciencia e Innovación (PID2019-111460GB-I00, ICTS-2017-28-UPV-9F, TEC2017-90556-RED1, FPU17/04224) and Generalitat Valenciana (PROMETEO/2019/123, IDIFEDER/2018/033) are acknowledged. The authors also thank Miroslavna Kovylyna for the optimization of the GST deposition process.

[1] S. Abdollahramezani <i>et al.</i> , <i>Nanophotonics</i> 9, 1189 (2020).	[6] H. Hu <i>et al.</i> , <i>Asia Comm. and Photonics (ACP)</i> , 1-3 (2018).
[2] Jorge Parra <i>et al.</i> , <i>Laser & Photonics Rev.</i> , 2000501 (2021).	[7] J. Feldmann <i>et al.</i> , <i>Nature</i> 589, 52-58 (2021).
[3] H. Zhang <i>et al.</i> , <i>Opt. Express</i> 29, 3503-3514 (2021).	[8] M. Wuttig <i>et al.</i> , <i>Nature Photonics</i> 11, 465-476 (2017).
[4] V. Srivastava <i>et al.</i> , <i>Nature Sci. Rep.</i> 10, 11131 (2020).	[9] C. Rios <i>et al.</i> , <i>Science Adv.</i> 5, 1-9 (2019).
[5] H. Zhang <i>et al.</i> , <i>Opt. Lett.</i> 43, 5539-5542 (2018).	[10] C. Rios <i>et al.</i> , <i>Opt. Mat. Express</i> 8, 2455-2470, (2018).

Spintronics
Photonics
Phononics
Magneto-Optics

CONTACT PERSON Email: pabsanki@ntc.upv.es